Optoelectrical and Photochemical Investigation of 2D Nanomaterials and their Nanocomposites Fabricated by Laser Ablation in Liquid

March 2021

DHONGADE SIDDHANT

Tokushima University
Graduate School of Advanced Technology and Science
Systems Innovation Engineering, Optical Systems Engineering
Doctoral Course

Abstract

Synthesis of In_2Se_3 nanocubes fabricated by laser ablation under DI water and its Field electron emission properties as well as the carrier dynamics were investigated successfully for the application of high current density cold cathode material. The morphological characterization carried out using field-emission scanning electron microscopy (FESEM) and transmission electron microscopy (TEM) reveal that the nano-cubes have an average size of 70 nm. The X-ray diffraction and Raman analysis clearly imply the formation of pure and crystalline In_2Se_3 phase only, without any impurity phases, despite the laser ablation being carried out in aqueous medium. A superior FE property characterized by lower values of turn-on and threshold fields as compared to In_2Se_3 nanowires emitter and ability to deliver very large current density ~2656 $\mu A/cm^2$ by applying the field of 9.7 V/μm. Transient absorption spectra reveals there are no deep trap levels, the electrons in nanocubes can be regards as mobile carriers through the hopping process and travel long distance in the absence of holes.

Carrier dynamics and photocatalytic performance of novel In_2Se_3/ZnO/Au-nanoparticle ternary composite system is investigated. The ternary photocatalytic system was fabricated using hydrothermal and laser ablation technique. The structural and physical characteristics have been studied by SEM, TEM, ultraviolet-visible (UV–Vis) spectrophotometry, and micro-Raman spectroscopy. The photocatalytic activity of the nanocomposites was estimated through the photocatalytic degradation utilizing organic dye of methylene blue in an aqueous solution. Results suggested that the ternary composite showed better photocatalytic performance compared with the pristine and binary composites.

Production of few layers graphene from graphite is fabricated by UV laser scanning method. Morphological, structural and optical properties were investigated by TEM, HRTEM, UV-Vis spectroscopy and Micro-Raman spectroscopy. The surface modification of graphite under different liquid environment was investigated by optical laser microscope. After laser scanning the holes in graphite surface becomes dipper and less wide. The laser scanning process is most effective process to remove the layers of the graphite plate. Dips and hill are modified after laser scanning.

Acknowledgment

My deep gratitude goes to Professor Akihiro Furube, who expertly guided me through my Ph.D. and who shared the excitement of 3 year of discovery. His unwavering enthusiasm for optical and material science kept me constantly engaged with my research, and his kindness and generosity helped me to learn more about optical science and physics behind it. He has been a great resource throughout the research. He has steered me in the right direction and give a great support throughout the work process by keeping me motivated. His calmness, his patience and quality of guidance gave me a lesson of life. ***古部昭広先生に心より感謝申し上げます。***

A special thanks to Associate Professor Pankaj Koinkar for his precious help from getting admission to throughout Ph.D. I am very thankful to Associate Professor Pankaj Koinkar for helpful discussion research advice continuous encouragement. I would also like to thank Dr. Tetsuro Katayama for his dedicated support and assistance providing advice regarding analysis many times during my PhD work.

I would also like to thanks our collaborator Professor Mahendra More, Miss Pallavi Mutadak and Mr. Amol Deore for their research contribution. I would like to express my gratitude to technical staff Mr. Satoshi Sugano and Mr. Tomoyuki Ueki for constantly supporting my experiments.

Furthermore, I would like to thank Government of India and Indian Embassy Tokyo Japan for the National Overseas Scholarships and constant financial and moral support throughout my Ph.D.

I also express my gratitude to Mr. Tadatake Sato and Mrs. Aiko Narazaki for their allowing to do internship in their (AIST) lab as well as their constant support during internship. I would also like to thank Mr. Yashiro, Mr. Kurozaki Mr. Kawaguchi and Ms. Kamiyama san for technical support throughout internship program.

I would like to thanks my friends and colleagues Mr. Yamaguchi, Mr. Okazaki, Mr. Yoshimoto, Mr. Mori, and all lab mates for their constant support.

Above ground, I am indebted to my parents Vijaya and Anand Dhongade, whose value grows with age. I also thanks to my uncle Mr. Ashok Ramtake and cousin Mrs. Trupti Ramtake Gawai for their moral support. Finally, I would like to thank Mrs. Ikuta for taking care of me in Japan, like a mother.

Dedicated to my supervisor Professor Akihiro Furube

CONTENTS

List of figures and tables

Chapter 1

Chapter 2

Chapter 3

Chapter 4

Chapter 5

Abbreviations

UV-Vis	Ultraviolet-visible
SEM	Scanning Electron Microscopy
TEM	Transmission Electron Microscopy
HRTEM	high resolution transmission Electron Microscopy
XRD	X-Ray Diffraction
fs	Femtosecond
UTAS	Ultrafast Transient Absorption Spectroscopy
AuNP	Gold nanoparticle
GSB	Ground State Bleaching
Nd:YAG	Neodymium-doped Yttrium Aluminum Garnet
MB	Methylene Blue
DMB	Degraded Methylene Blue
FWHM	Full Width Half Maximum
TMD	Transition metal dichalcogenides
PLAL	Pulse laser ablation in liquid
rGO	Reduce graphene oxide
FED	Field emission display
DI	De-ionized

Chapter 1: Introduction

1.1 A brief introduction of 2D material

The research on two dimensional (2D) nanomaterials are getting extensive in recent years due to their unique optical, optoelectronics, electrical, magnetic properties. The 2D materials are single layered sheet like structure. The journey of 2D materials started with graphene and now there are more than 50 combinations of 2D materials. Figure 1 shows the general classification of 2D materials, there are 8 classes which includes the graphene family, 2D metals, h-BN, COF, BP, oxides, MXenes, TMDs, LDHs and MOFs. 2D materials become a research major among the broad applications in the field of electronic, medical, and chemical field. The phonons and electronic structures of 2D material vary between bulk and nanoform[1-7].

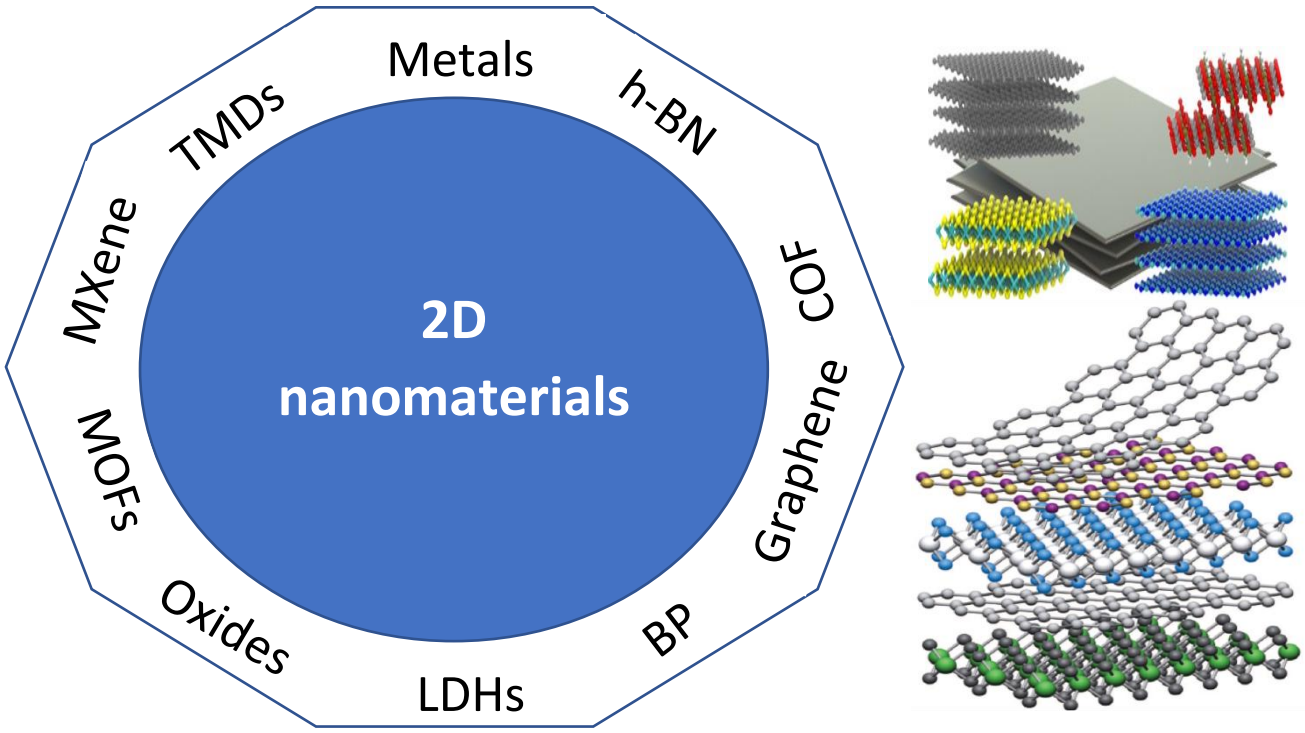

Figure 1: Classification of 2D material with layered structure and models[8].

https://imechanica.org/node/17999

The nanoforms exhibit special and interesting properties different from their bulk phases due to quantum confinement of electron and having no interlayer interaction[9-11]. Usefulness in electronic and optoelectronic devices is due to outstanding electron transport performance with great mobility at room temperature[12, 13]. Although 2D nanomaterials are promising materials for great performance in electronic and optoelectronic devices, other properties of 2D nanomaterials should be examined for various applications[5, 14, 15] .

1.2 Indium selenide

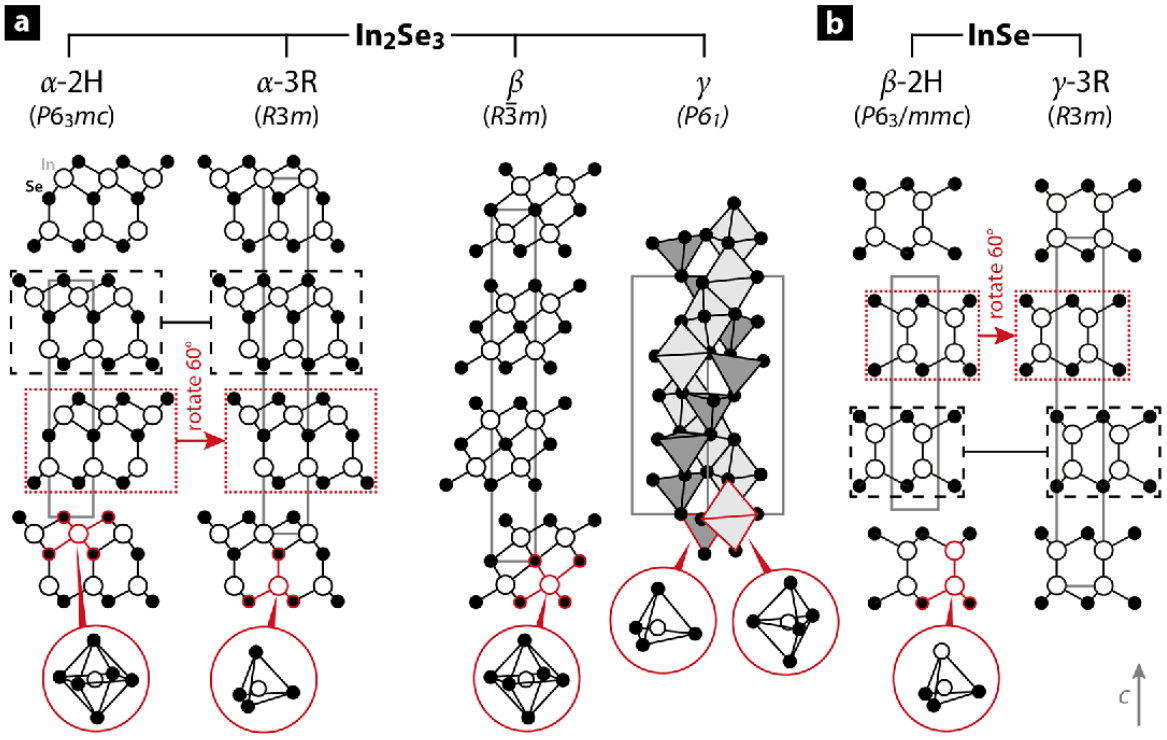

Figure 2: Indium selenide phases, crystal structure, symmetry and orientation[16]

Indium selenide (In_2Se_3) is black colored III-VI binary n-type semiconductor accompanied by the formula M_2X_3 having a layered structure. Indium selenide is found in some significant phases like

α, β, γ, δ and κ having different bandgap energies and shows varied optical properties[17, 18]. Figure 2 shows the illustration of phase crystal structure symmetry and atomic orientation of indium selenide. Furthermore, thermodynamically α-In_2Se_3 phase comprises of two individual staking variants as 2H and 3R phases. Both the α(3R) and α(2H) In_2Se_3 possess three-layered rhombohedral structure accompanied by the space group $R\bar{3}m$ and two-layered hexagonal structure having space group $P6_3$ respectively[19]. The α-In_2Se_3 nanosheet reveals powerful covalent bonds along the planer lattice of layered structure and weaker Van der Waals interaction between adjacent layers which shows the enhanced carrier mobility. Indium selenide has a narrow and tunable direct bandgap, high absorption coefficient, broad response range, and high sensitivity[20]. Many past pieces of research have illustrated that many optical and electrical properties of In_2Se_3 nanostructures are size and morphology dependent. Because of its attractive electrical, optical, magnetic, and polymorphic properties, In_2Se_3 has many potential applications as phase-change random access memories, photovoltaic application, field emission devices and so on[21-23].

1.3 Graphene

Graphene is a 2D layered carbon arranged in a honeycomb lattice. Graphene is a semiconductor where as its 3D relative, graphite is a semimetal in nature. Figure 3 shows the appropriate illustration of Graphene. Graphene has hexagonal honeycomb like structure where carbon atoms are placed in each corner and each carbon atoms are connected with σ- bond[6, 24, 25]. Mechanical exfoliation (Scotch-tape method) was the first method to obtain the few layers and single layer graphene, epitaxial chemical vapor deposition also another method to synthesize graphene but both methods are expensive and less effective for large scale manufacturing. There are several chemical root methods to synthesize graphene like hummers methods, advanced hummers method, hydrothermal synthesis and so on[26-31].

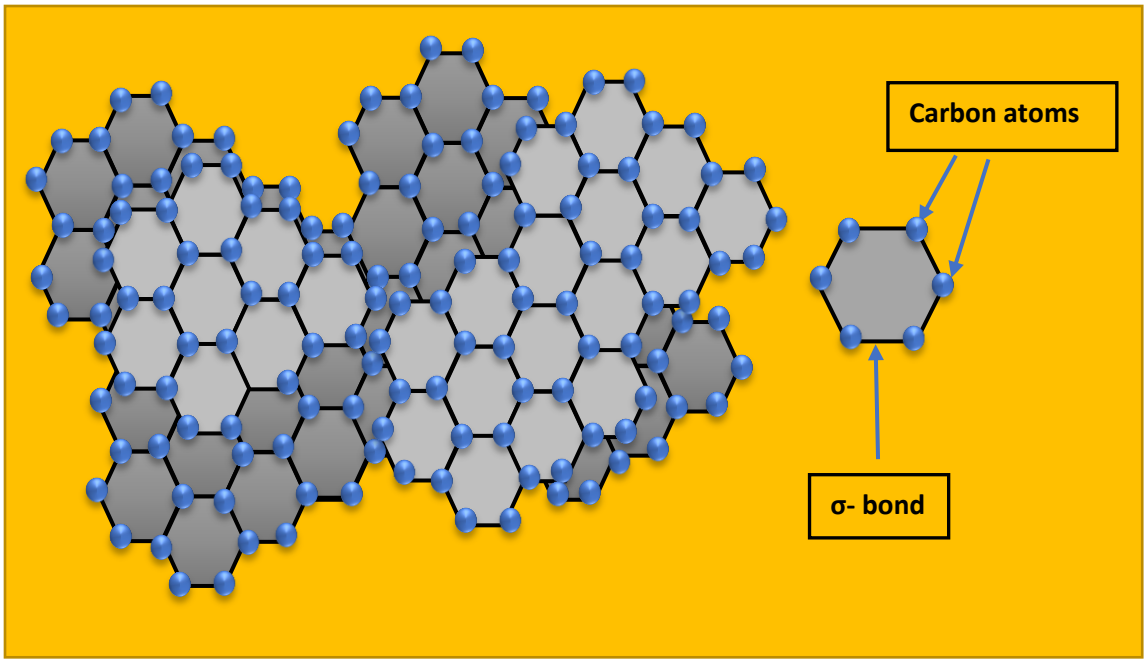

Figure 3: 2D graphene sheet with carbon atom in each corner and carbon atoms are connected with σ- bond.

Compared with other 2D materials, graphene is more environment friendly, biocompatible and photostable. Due to its ~0 eV bandgap with excellent optical properties, graphene is highly desirable for various applications like photocatalysis, solar cell, biosensing and light emitting diode (LED)[24, 27, 32-34].

1.4 Gold nanoparticles (AuNP)

Gold is widely used material in optical, chemical and medical research. Due to the exceptional optical properties of small AuNP, their high chemical stability and electrochemistry influenced by size have given opportunity to the researcher to explore AuNPs application in the field of biolabeling, catalysis, electron-transfer theories, phase transfer, DNA melting and assays, and crystal growth[35-41]. The spherical AuNP colloid is usually intense red in color and changes its color towards blue or purple as size increases. AuNP can be synthesized by various chemical methods

such as Turkevich method, using capping agent, Brust-Schiffrin` method, martin method and Sonolysis[42-46].

1.5 Zinc Oxide (ZnO)

Recent decade shows intense research going on ZnO and its application in various fields. With wide band bap of 3.37 eV at room temperature, ZnO crystallizers found in two main forms, Hexagonal wurtzite and cubic Zincblende. ZnO is a soft material having hardness 4.5 on Mohs scale with high heat capacity and heat conductivity, low thermal expansion and high melting temperature[47-49].

ZnO nanostructure have a large surface area and high catalytic activity. The physical and chemical properties of ZnO is depends on the morphology of ZnO nanostructure. To develop different morphology, many synthesis methods are developed such as combustion method, hydrothermal method, electrochemical deposition, sol-gel method, thermal decomposition, laser ablation and so on[50-57].

1.6 Pulse laser ablation

Pulse laser ablations in liquid (PLAL) is a promising and low-cost method among all synthesis processes, because of its unprecedented advantages such as environmental sustainability, effortless experimental setup, long-lived stability of nanoparticles, tuning of desired phase formation, and no production of any harmful reactant or contamination. This is a kind of physical method for the production of various morphological nanostructures[58]. The fabrication of nanostructures possessing various morphologies is achieved by managing the characteristic of laser ablation environment, pulse width, wavelength, spot size, fluence, and power of experimental laser[59]. In

PLAL method, a Q-switched Nd: YAG laser (wavelength ~ 532 or 1064 nm) is commonly used. however, few reports showed that 266 nm wavelength laser has been used to synthesize nanoparticle[60, 61].

1.7 Ultrafast carrier dynamics

1.7.1 Principle

The ultrafast transient absorption spectroscopy (UTAS) is the technique to observe energy and carrier transfer in an optical nanomaterial. This process commonly takes place on a very short time scale, from tens of fs to hundreds of ps. In this method pulse laser used to excite a nanoparticle electron from their ground state to a higher energy state. A probing light is white light source, used to obtain an absorption spectrum of a nanomaterial at time scale of picosecond. Ultrafast optical spectroscopy has been widely used to investigate the electron-phonon dynamics[62, 63].

1.7.2 Transient absorption spectrometer

1.7.2.1. Diffuse reflectance femtosecond transient absorption spectroscopic setup

Figure 4 show the optical set-up of diffuse reflectance ultrafast transient absorption spectroscopy. The light titanium sapphire source with a regenerative amplifier (Hurricane, spectra physics) having 800 nm of wavelength, 130 fs FWHM pulse width 0. 8 mJ pulse^{-1} and repetition of 1KHz used for the spectroscopic measure. The fundamental laser beam cuts into two and one of them used to as pump light after converting to the second harmonic of 400 nm wavelength at 500 Hz

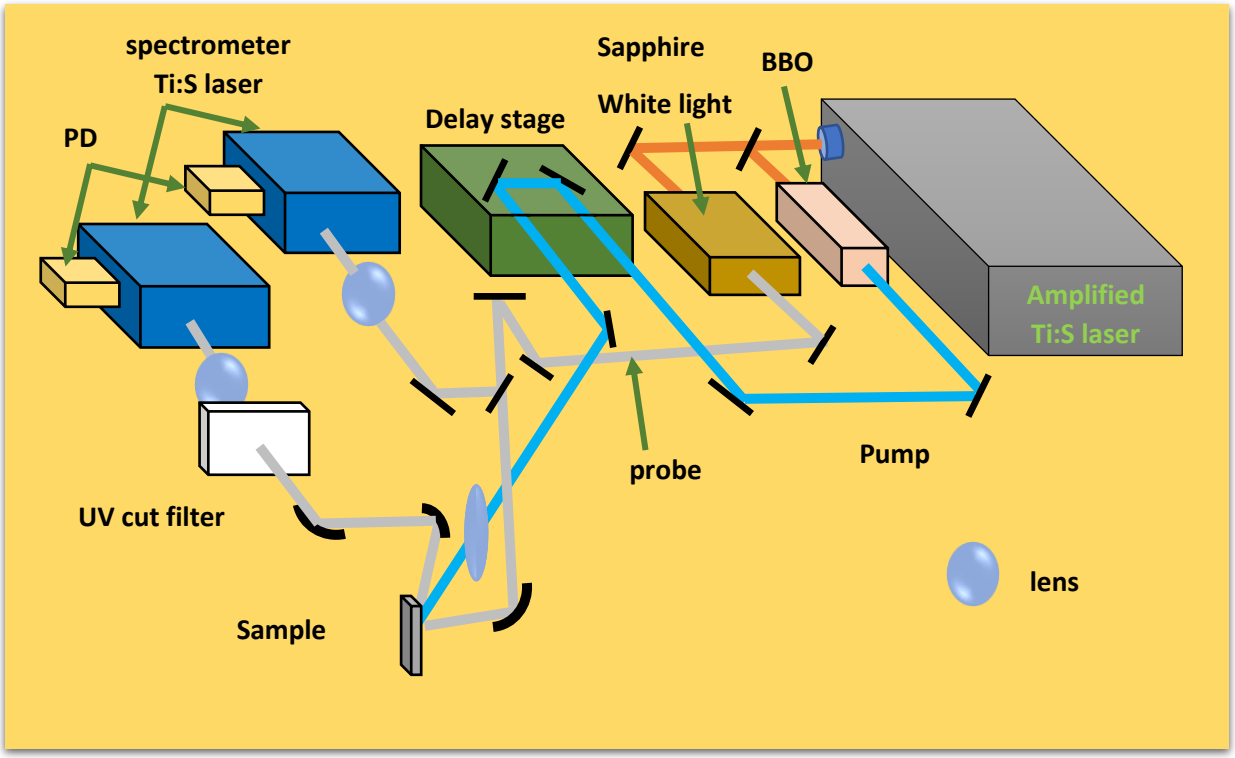

Figure 4: Optical set-up of UTAS at diffuse reflectance system

modulation frequency. The 2nd beam is converted into white light by focusing in to sapphire plate (2 mm) use as a probe light. both pump and probe were focused on the sample. The diffuse reflected probe light was perceived by silicon photodiode after passing through a monochromator. Transient absorption intensity was calculated by formula %Abs. = $100(R_0-R)/R_0$, where R_0 and R were diffuse reflected probe light intensity without and with excitation, respectively[64].

1.7.2.2. Femtosecond Transient Absorption spectroscopic setup

Figure 5 well illustrate the ultrafast femtosecond Transient Absorption spectroscopic setup. The Solstice, Spectra-Physics 1KHz having 3.5W power femtosecond laser used as a laser source. The second harmonics at 400 nm was used for pump pulse. Transient absorption spectra were probed

by delayed pulses of a femtosecond white-light continuum, generated by focusing a signal light pulse (1200 nm) from OPA (TOPAS, Light Conversion) into a CaF_2 plate. Probe light was detected by a C-MOS multichannel detector (Hamamatsu, PMA-20). The temporal resolution was ca. 150 fs[65]

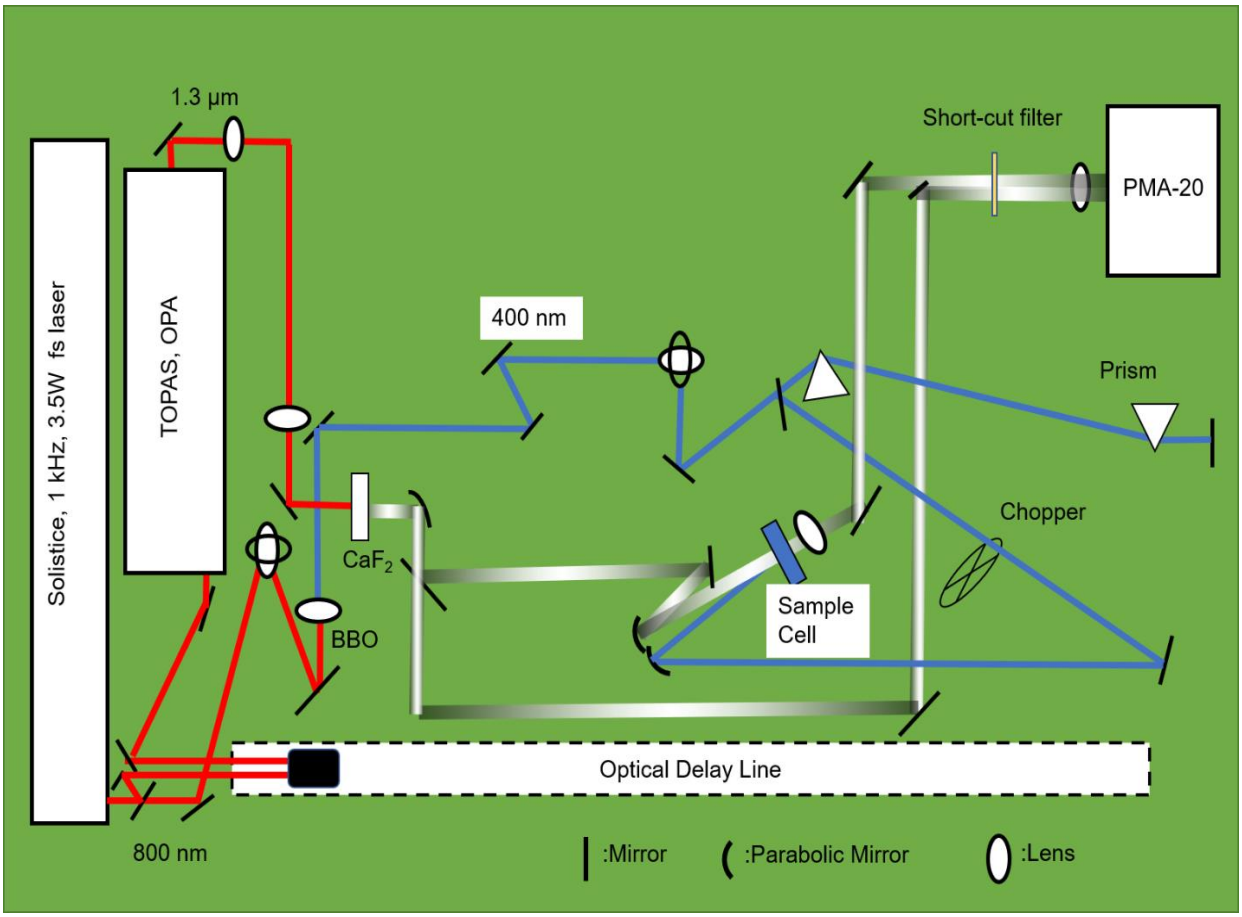

Figure 5: Ti:S femtosecond Transient absorption spectroscopy

1.7.3 Aspects of Absorption Spectra

Transient Absorption spectra: At a fixed delay time of pump and probe, TA spectra were measure by scanning the detection monochromator in a spectral region of 400-2000 nm. After

optical excitation the wavelength shows the eighter positive or negative amplitude, they called excited state absorption and ground state bleaching respectively.

Ground state bleaching: the loss of ground state absorption due to excitation of molecules causses transmittance of the probe is increased and the negative band is measured. This signal is formed within a pump pulse and lasts until the ground state of molecules gets repopulate.

excited state absorption: The positive absorption changes due to the transition of molecules from the initially excited state to some higher state which is formed within the pump pulse.

1.8 Field electron emission

1.8.1 Introduction

To eject the electron, form the surface of the material in to the vacuum which requires the critical energy called work function (ϕ) and the process is called the field electron emission. Field-electron emission is also known as cold emission, which is purely a quantum mechanical tunneling phenomenon[66, 67].

1.8.2 Principle

In this process, electrons tunnel through the surface potential barrier in the presence of an applied electric field[25]. The field emitters (cold cathodes) advantageous/superior than the hot cathodes and practically employed in various vacuum microelectronic devices. Figure 6 shows the ejection of an electron from the metal surface in presence of the electrical field in vacuum[68-71].

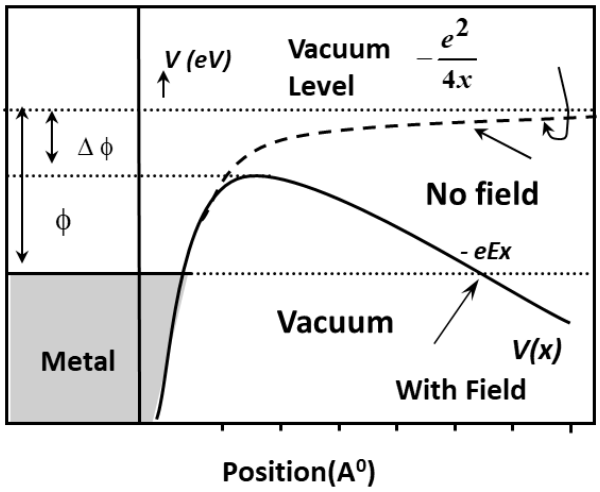

Figure 6: Illustration of field emission from metal surface with and without field[72]

1.8.3 Fowler-Northeim theory and its validation

The field emission from the metal is well described by the fowler Northeim model which is developed by the theorist R. H. fowler and L.W. Northeim in 1928. The model is based on the four assumptions[25, 73-75].

1. The temperature of the metal is 0 K.
2. The electrons in the metal follows the free-electron approximation
3. The surface is smooth and planner
4. The potential barrier near the surface consists of the image force and the applied electrical field.

The modified F-N theory for the laser number of nanostructure emitter is as follows

$$j = \lambda_m \phi^{-1} E^2 \beta^2 exp\left(-\frac{b\phi^{\frac{3}{2}}}{\beta E} v_f\right)$$

Where j is emission current density, E is the applied average electric field, φ is the work function, v_f is value of the principle Schottky Northeim barrier correction factor and β is field enhancement factor.

1.9 Photocatalysis

1.9.1. Introduction

Photocatalysis is a branch of chemistry which deals with chemical reaction under the light in presence of photocatalyst. Photocatalysis has a wide range implementation such as water purification, hydrogen production, oxygen production, deionization, antibacterial and self-cleaning. The energy consumption of the world increases exponentially with the rise in population and standard of living, to satisfy the global demand requires a clean renewable energy source, and the hydrogen is a great candidate for the such a global requirement. From 1972 hydrogen production using photocatalysis stimulated great research interest. Photocatalysis is an economical route of for hydrogen production using natural resources water and light[76-78]. One of the promising methods to produce hydrogen via photocatalysis is the light induced photo-oxidation of water using metal oxide as a photocatalyst such as TiO_2 and ZnO[79-82].

1.9.2. Principle

Photocatalysts is a semiconducting material, which enhances the rate of reaction using its surface area and charge transfer properties under light. when a photon involves in a reaction, the system becomes a photocatalytic system. The catalysts took action by absorbing the reactant and by absorbing photon photons which create electrons and holes, responsible for the redox reaction.

1.10 Purpose and significance of the research

Despite being an important metal chalcogenide, there are very few reports on FE characteristics of In_2Se_3 nanostructures. As stated in the earlier section, the FE properties exhibit noticeable dependence on the overall morphology of the nanostructures, in addition to their electronic properties (carrier density, mobility etc.) In this regard, it is of scientific and technological importance to reveal the FE behavior of In_2Se_3 nano-cubes and perform the UTAS analysis to understand the carrier behavior, which hitherto are not attempted. In this research article, we demonstrate the synthesis of nearly mono-dispersed In_2Se_3 nano-cubes using simple laser ablation in liquid ambient for superior field emission. An attempt has been made to exemplify the growth of the In_2Se_3 nano-cubes. The as-synthesized In_2Se_3 nano-cubes have been characterized to reveal their crystal structures, morphology, optical and electronic properties using XRD, SEM, TEM, micro-Raman PL, and UTAS, prior to field emission characterization. Our results show that the In_2Se_3 nano-cubes emitter has superior FE characteristics, competency to deliver very high emission current density (~2656 $\mu A/cm^2$) at a moderate applied field (9.7 V/μm), and very good emission stability over the duration of 5 hours.

A noble photocatalyst In_2Se_3/ZnO/Au-nanoparticle (AuNP) ternary system was developed via a simple hydrothermal process and laser ablation process. The substantial carrier dynamics of the ternary system were performed using pump-probe ultrafast spectroscopy and later we checked its substantial performance using photocatalytic reduction of methylene blue dye. The great photocatalytic reduction activity of ternary composite attributed to charge transfer among In_2Se_3, ZnO and AuNP. The ZnO facilitates the charge carrier separation and migration in the ternary catalytic system. Ultimately, a potential charge carrier mechanism of photogenerated charge carriers over the In_2Se_3/ZnO/AuNP ternary composite system is proposed.

In this research, we discussed about the graphene and its production using ultra-violet laser light scanning of graphite. The approach is to remove upper single layer or few layers of the graphite to produce high quality of graphene. The scanning 266 nm UV laser was used to mechanically remove the upper layers of graphite. To reduce the damage, the UV laser was focused 0.2 mm below the surface of the graphite plate.

.

Chapter 2: Experimental

2.1 Synthesis of In_2Se_3 nanocubes

In_2Se_3 cubical nanostructures were prepared by the laser ablation in a liquid environment. In the experimental process a Q-switched Nd:YAG nanosecond laser (Spectra Physics Quanta-Ray) having pulse duration ~ 10 ns (FWHM), wavelength ~ 532 nm, pulse power ~62 mJ, and repetition frequency ~ 10 Hz, was used as the laser source. The laser fluence was kept about 0.31 J/cm^2. The 20 mg of In_2Se_3 microcrystalline powder (Sigma Aldrich) was dispersed in 20 ml double-distilled (DI) water via ultrasonication. The In_2Se_3 dispersion in DI water was subjected to laser ablation (laser power ~620 mW) performed for 20 min duration. After completion of the laser ablation, the final product was dried overnight in a hot air oven with a constant temperature at 120 ^{0}C.

Morphology of the In_2Se_3 was investigated using field emission scanning electron microscopy (FE-SEM) (JEOL JSM -6510A, Japan) and transmission electron microscopy (TEM) (JEOL JEM-2100F, Japan). TEM and FE-SEM were operated at 200 kV and 5 kV, respectively. The binding energy of an electron in the orbital of obtained In_2Se_3 was characterized by X-ray photoelectron

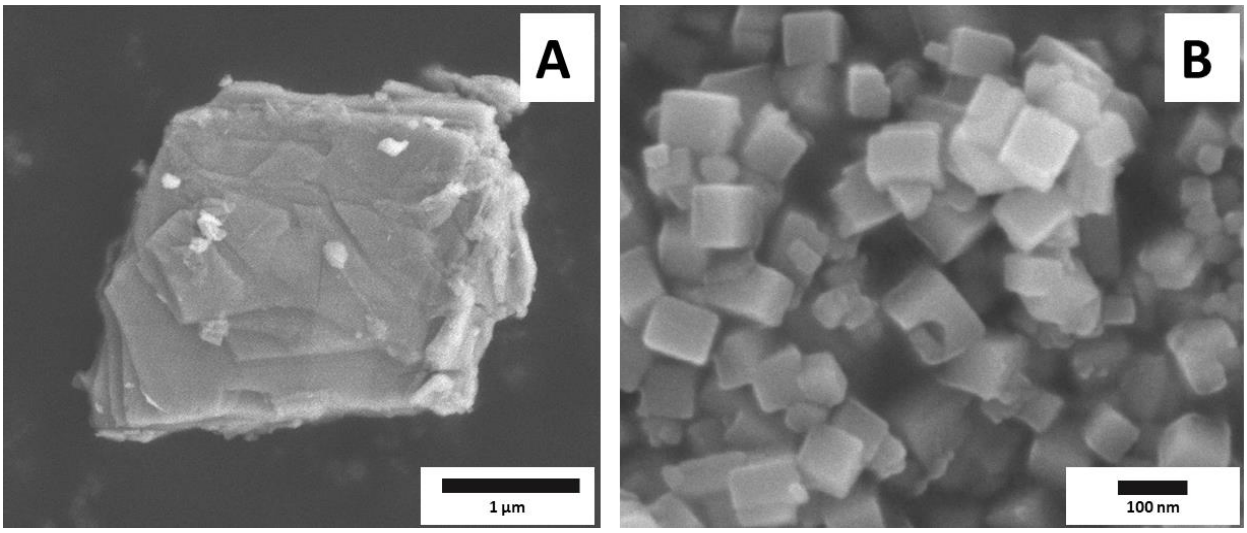

Figure 7: SEM images of (A) bulk In_2Se_3 and (B) In_2Se_3 cubes after laser ablation in water

spectroscopy (XPS) (ULVAC-PHI, Inc.) with X-ray source Al-Kα (1487 eV) at room temperature. The UV-visible spectra of bulk (as-received microcrystalline powder from Sigma Aldrich) and laser-ablated In_2Se_3 were taken using the V-670 (JASCO-Japan) spectrometer as well as the Raman spectra were taken using Renishaw microscope operating at 532 nm.

The FESEM images of bulk In_2Se_3 (as received from Sigma Aldrich) and the product harvested after laser ablation are depicted in figure 7. The surface morphology of as-received sample (figure 7(A)) is characterized by stacks of sheets. It is also showing the uneven irregular morphological microstructure with the uneven size of sheets in the stacks. Upon laser ablation, the formation of In_2Se_3 well-faceted nano-cubes is clearly seen from figure 7(B). The cubical nanostructures have an average size of ~ 70 nm. The change in surface morphology is a time-dependent phenomenon. A plausible mechanism of formation of In_2Se_3 nano-cubical structures is presented in a later section.

2.2 Synthesis of In_2Se_3/ZnO/Au (nanocubes, binary and ternary) nanocomposites

The laser source used for the synthesis of In_2Se_3 nanostructure and its composite was Q-switched Nd:YAG nanosecond laser (Spectra-Physics Quanta-Ray) having pulse duration ~10 ns [full width half maximum (fwhm)], wavelength ~532 nm, pulse energy ~55 mJ, and repetition frequency ~10 Hz. The fluence of the Nd: YAG laser is kept around 0.28 J/cm^2. The commercial microcrystalline indium (III) selenide (In_2Se_3) powder (Sigma Aldrich) and zinc oxide (ZnO) was used as the base material.

(A) Synthesis of In_2Se_3 nanocubes and its composite with AuNP

Our previous research describes the synthesis of In_2Se_3 nanocubes using laser ablation in deionized water (DI) water[83]. The In_2Se_3 cubical structure and its composite with AuNP (In_2Se_3/Au) were

prepared by laser ablation in a liquid environment. The 20 mg In_2Se_3 microcrystalline powder were dissolved in the 20 ml DI water and Au colloidal solution[40] respectively, each solution was treated by 10 minutes probe ultra-sonification and 20 minutes normal sonification. Afterward, both samples were mixed and laser-ablated for 20 minutes. The supernatant of laser-ablated samples was further investigated by various characterization.

(B) Synthesis of In_2Se_3, ZnO composite and AuNP decoration

To prepare the binary composite of In_2Se_3 and ZnO (In_2Se_3/ZnO), 18 mg In_2Se_3 and 2 mg ZnO were dissolved in DI water. To prepare the ternary composite of In_2Se_3, ZnO, and Au (In_2Se_3/ZnO/Au), 18 mg In_2Se_3 and 2 mg ZnO were dissolved in the mixture of DI water and Au colloidal solution. Both samples were treated with 10 minutes probe ultra-sonification followed by 20 minutes of simple ultra-sonification. To mix each sample, both samples were put into the hydrothermal reactor (HTR) for 18 hours at 180^o C. Subsequently, mixed samples were laser ablated for 20 minutes as illustrated in Figure 1, and the supernatant is taken for further investigation.

2.3 Synthesis of Graphene

To prepare few layers graphene (FLG) 1 mm X 1 mm graphite plate was cut out from 5 mm X 5 mm graphite plate having thickness 0.2 mm. The 266 nm UV laser having 127 mW power was used for the laser ablation. to reduce the damage to the graphite, plate the focus of the laser set at the 0.2 mm below the graphite plate. The UV laser light was propagated through the laser scanner which is driven by the simple line program. The scanning ablation was performed under different liquid environments such as water, ethanol, methanol, Isopropyl alcohol (IPA) and 50% water + 50% Ethanol. After 3 hours of scanning the liquid was investigated by using UV spectrometer,

TEM, HRTEM, Raman spectroscopy, and scanned graphite plate was investigated using the optical laser microscope.

2.4 Transient absorption spectroscopy

UTAS measurements for powder samples were carried out using a femtosecond Ti:Sapphire laser with a regenerative amplifier (Hurricane, Spectra Physics, 800 nm, 130 fs, 1 mJ/pulse, 1 kHz). The details of the experimental principle and the apparatus are described in earlier publications[84]. The second harmonic (400 nm) was used for excitation. The pump beam diameter on the sample surface was about 0.4 mm. The probe beam was a white light continuum generated by focusing a part of the fundamental from the Ti:Sapphire laser into a sapphire plate (2 mm thick). The diffuse reflected probe beam was then detected with a photodiode after passing through a monochromator (Acton Research, SpectraPro-150). The %Abs. values were calculated based on the photodiode signals (typically 1000 shots) using a computer. The transient absorption intensity is calculated as % Abs. = $100(1 - R/R_0)$, where R_0 and R are reflected probe light intensities without and with excitation, respectively. The instrument response was < 1 ps.

2.5 Field electron emission

The FE measurements of In_2Se_3 nano-cubes, were performed in 'planar diode' configuration, at the base pressure of ~$1x10^{-8}$ torr as shown in figure 8. For FE studies, the field emitter was prepared by sprinkling a small quantity of In_2Se_3 nano-cubes powder onto a piece of 0.5 cm x 0.5 cm conducting carbon tape. The carbon tape coated with In_2Se_3 nano-cubes was then pasted onto a copper holder, attached to a linear motion drive. A phosphor coated tin oxide glass screen was used as an anode. The distance between the cathode and anode was kept constant ~1 mm. The emission current of the cathode was measured using Keithley electrometer by sweeping applied

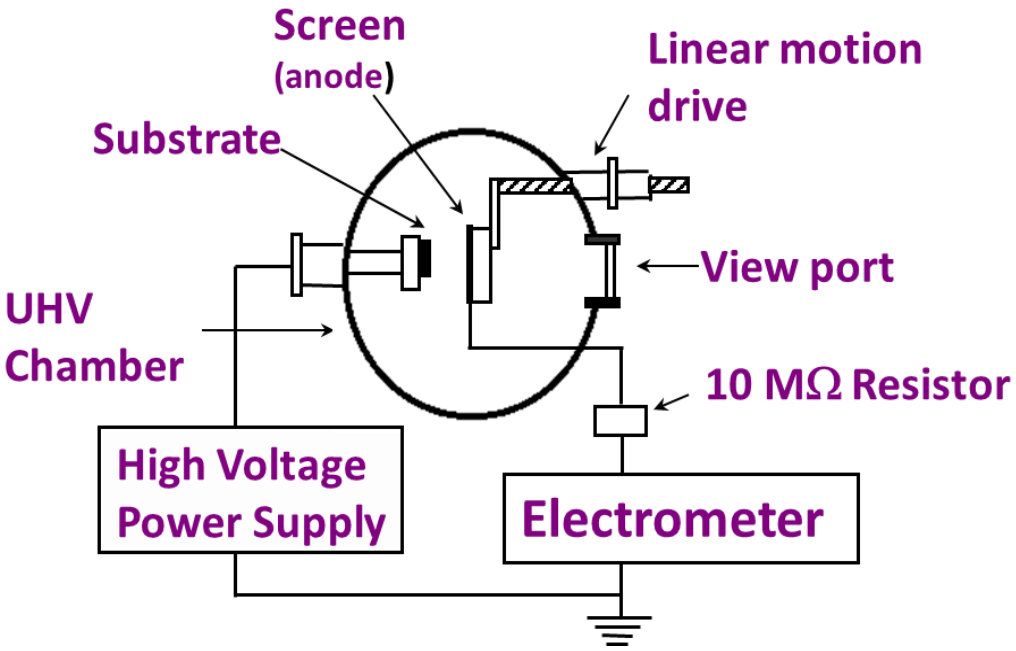

Figure 8: Field emission measurement setup[72]

DC voltage with a step of 40 V (40 kV, dual polarity, Spellman power supply), while the FE current stability was recorded using a computerized data acquisition system with an interval of 10 seconds. In order to ensure the reproducibility, FE measurements were performed on at least three different samples prepared under identical conditions.

2.6 Photocatalysis

The photocatalytic performance of In_2Se_3 and its binary and ternary composite was estimated by the degradation of organic dye. The methylene blue (MB) dye was used as the organic dye for the photocatalytic experiment. A photocatalytic reduction experiment was performed in a setup carrying a Xenon lamp with ultraviolet cut-off filter ($\lambda > 420$ nm) as a visible source installed at 7 cm from the photocatalytic cell. For a characteristic experiment, 400 µl supernatant of laser-ablated material was added to a 4 ml aqueous solution of MB suspension. Before illumination, to create

adsorption-desorption equilibrium, the solution was stirred magnetically for 15 minutes in the dark, and the concentration of solution before as well as after illumination was measured by UV-Vis-NIR spectrophotometer.

Chapter 3: Ultrafast carrier dynamics and field electron emission measurement of In_2Se_3 nanocubes

3.1 TEM and HRTEM analysis

Figure 9 depicts TEM and HRTEM images of the bulk and laser-ablated samples. The TEM image of bulk sample (figure 9(A)) shows uneven contrast on the particle surface, indicating that the

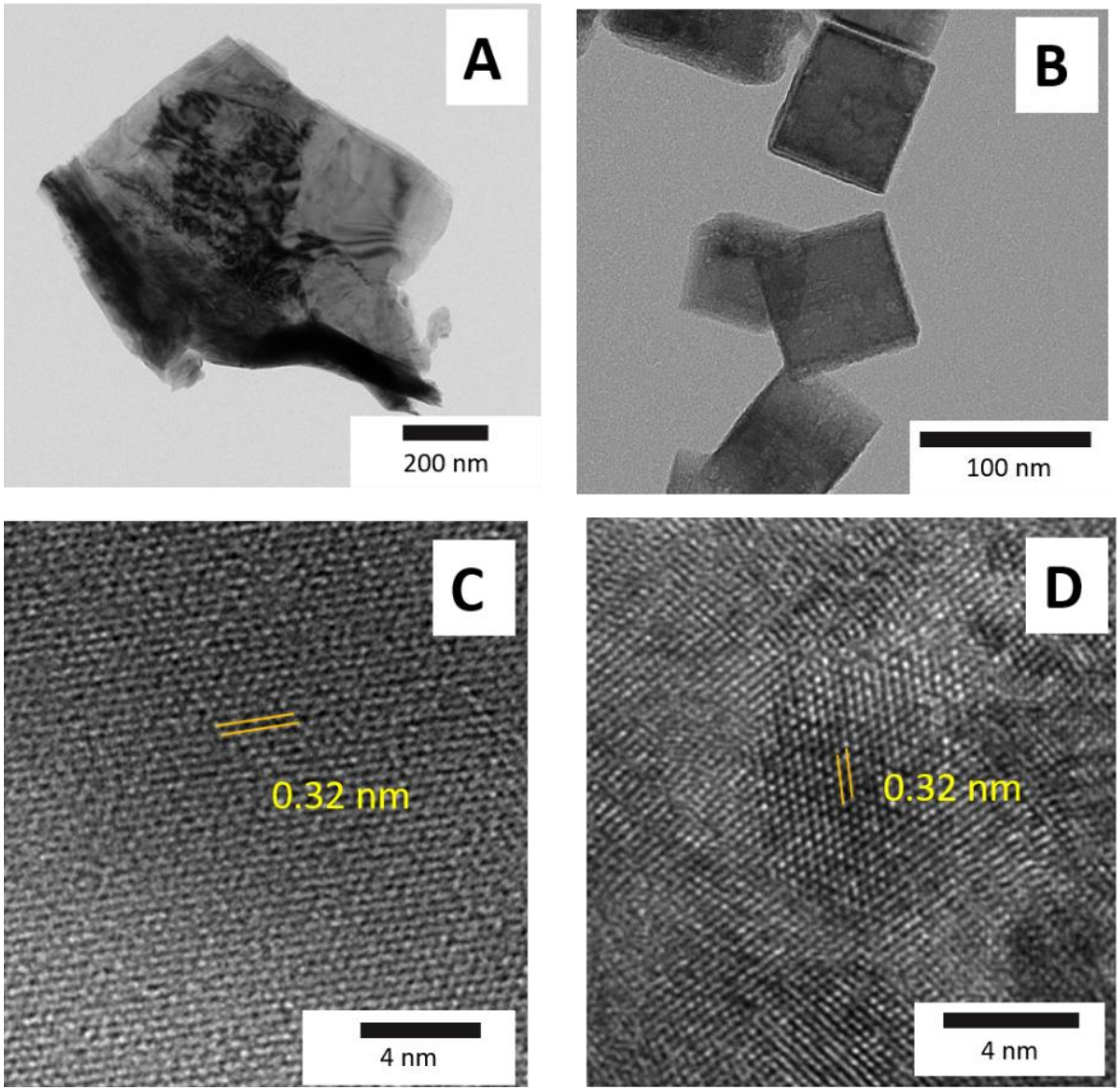

Figure 9: TEM and HRTEM images of In_2Se_3 (A) bulk In_2Se_3 with a layered structure and uneven surface (B) after 20 minutes laser ablation in liquid with scale 200 nm, (C) HRTEM before laser ablation in liquid (D) HRTEM image after laser ablation in water.

particle is a multi-layered structure with improper thickness, shape, and rough surface. A typical TEM image of In2Se3 structures harvested after laser ablation (20 min laser exposure) clearly shows their nanometric dimensions (figure 9B). The color contrast of the cubical particle is uniform, which suggests that the particle surface is even and an improvement in particle defects. The respective HRTEM images (figure 9 C and D) reveal the crystalline nature of both the samples, before and after laser ablation in water. The lattice spacing of ~0.32 nm corresponds to (100) crystalline plane of In_2Se_3.

3.2 Micro Raman and XRD analysis

the structural properties of pristine and laser-ablated harvested In_2Se_3 nanostructures, micro-Raman spectroscopic characterization was performed, and figure 10 A depicts the corresponding Raman spectra recorded at room temperature. Both the samples show characteristics phonon modes of pure In_2Se_3. A careful observation of the Raman spectra reveals that the laser-ablated In_2Se_3 sample shows a shift in all longitudinal optical (LO) and transverse optical (TO) modes towards lower wavenumber. It is because of the appearance of soft phonons, attributed to the formation of the nano-cubes. After laser ablation in water, the selenium nanocluster might be decomposed, so the laser-ablated sample shows all active modes frequencies near theoretical values[85]. According to the literature, the assignment of observed modes is shown in the graph. The A^1_1 is an active mode appearing due to longitudinal optical (LO) + transverse optical (TO) splitting (α-In_2Se_3). This also shows there is no phase change after laser ablation in water. The E type mode is observed in both samples with slightly different frequency. The A^2_1 mode was observed due to transverse optical (TO) phonon, whereas the assigned A^3_1 peak shows active mode coming from longitudinal optical (LO) phonon. The observed peaks in figure 10 B show In_2Se_3 bulk and

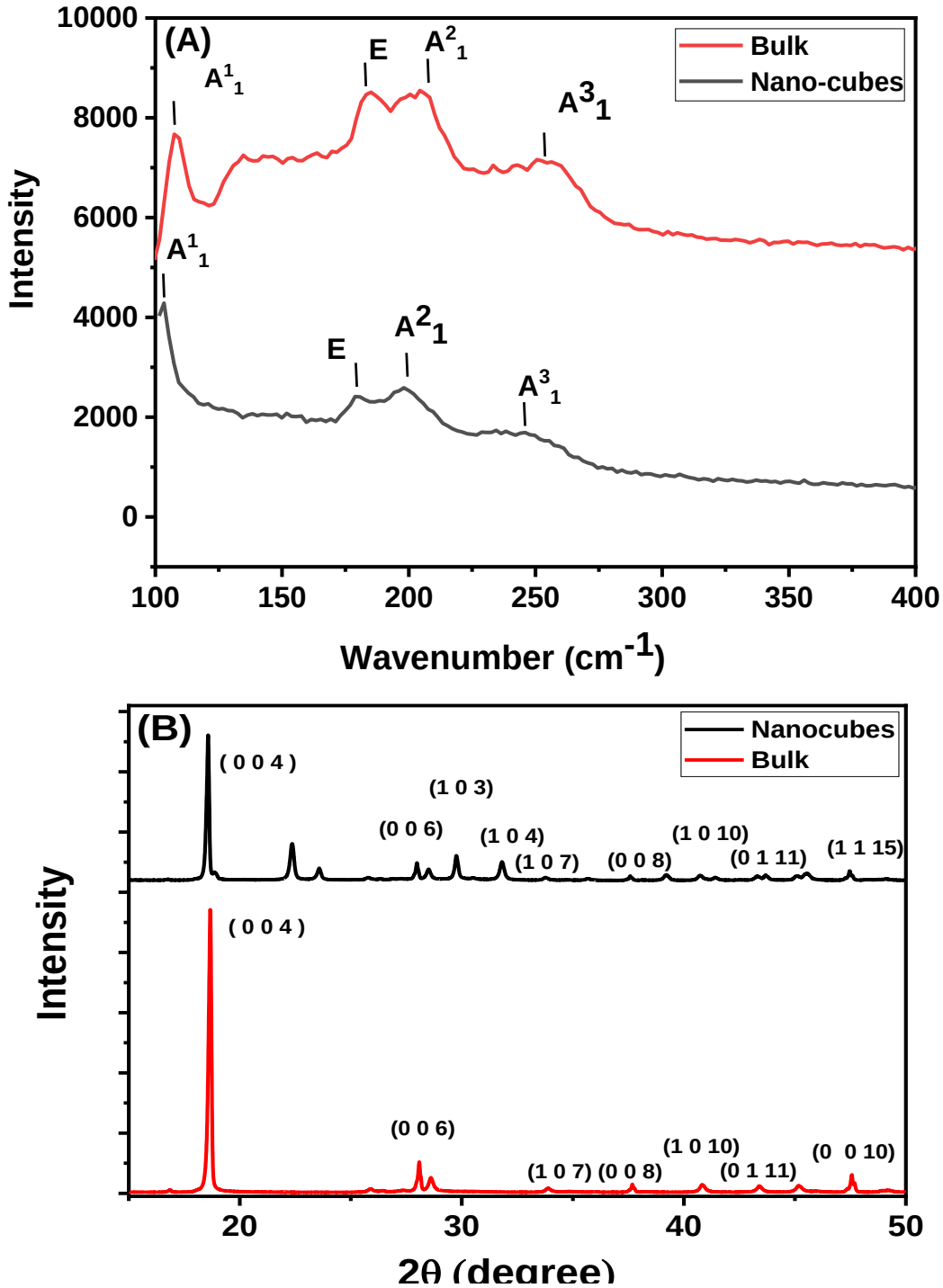

Figure 10: (A) Raman spectrum of bulk In_2Se_3 and nano-cubes In_2Se_3 and (B) XRD spectrum of In_2Se_3 nanocubes.

nanocubes sample which corresponds to the α phase of In_2Se_3. It is clearly indicating that there is no phase change after laser ablation. Each sample shows hexagonal symmetry with space group

P63/mmc (194) (JCPDS no. 00-034-1279).

3.3. Growth mechanism of In_2Se_3 nanocubes

The evolution of nano-cubical structures upon laser ablation in aqueous medium is schematically depicted in figure 11. For this, FESEM characterization of the samples harvested after laser ablation carried out for 5, 10, 15, and 20 minutes, was carried out. The FESEM images clearly show that there is a drastic change in the overall morphology of the resultant product with respect

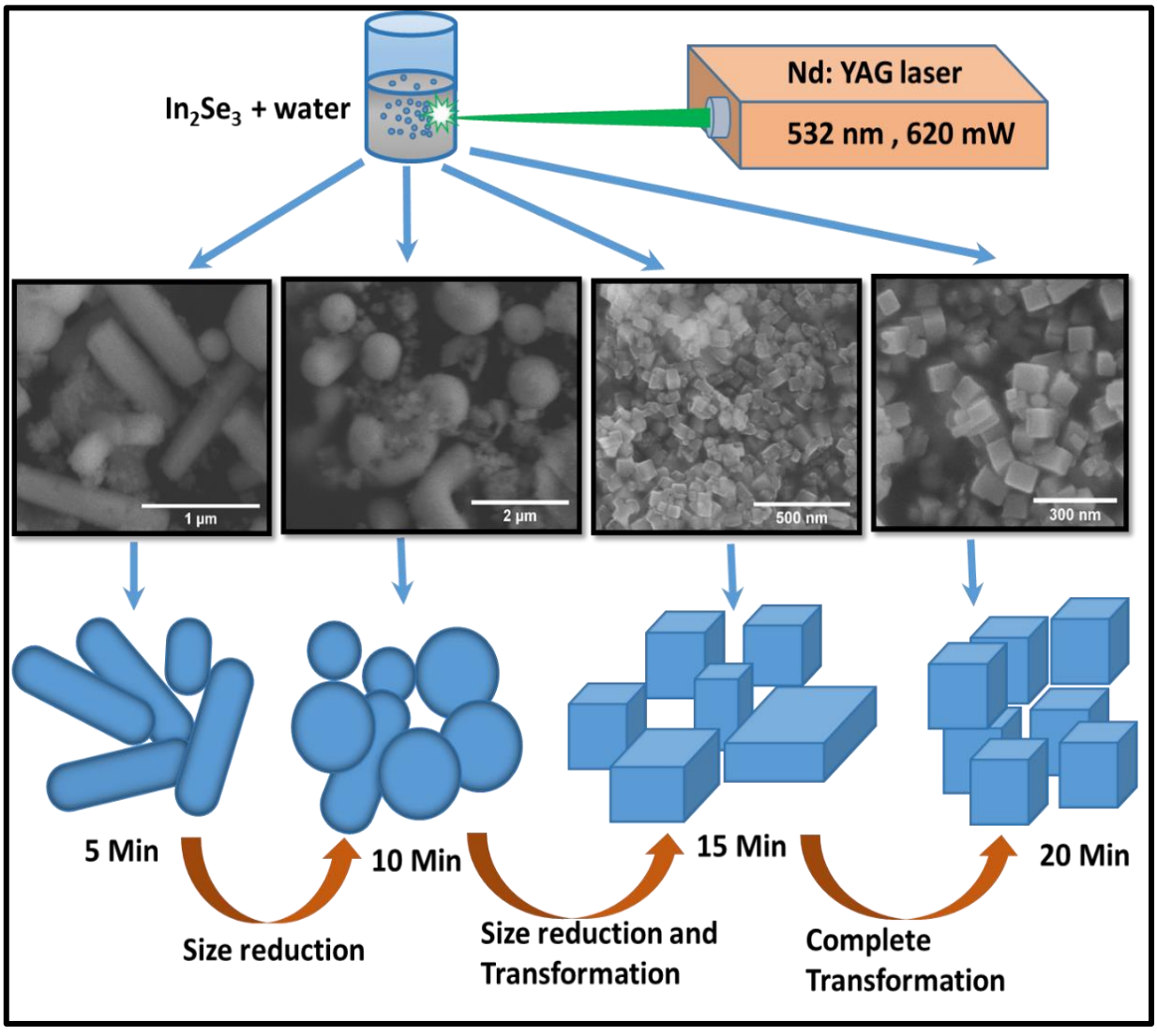

Figure 11: Growth mechanism of nano-cubes of In_2Se_3 ablated for 5,10, 15, and 20 minutes

to ablation duration. When the ablation was carried out for 5 minutes duration, the formation of rod-like structures (having a diameter less than 300 nm and length in few microns) is observed. With increasing the ablation time to 10 minutes, most of the rod-like structures are transformed into spherical particles with a diameter ~ 800 nm. When the ablation duration was increased to 15 minutes, initiation of formation of cubical nanostructures having an average size ~ 100 nm is observed. When the ablation was carried out for 20 minutes, formation of well facetted nano-cubes was observed. It is interesting to note that with the increase in the ablation duration, in addition to the noticeable change in surface morphology (rods to spherical particles to nano-cubes), a reduction in the average size of the resultant structures is observed.

The variation in overall surface morphology and reduction in the size of the resultant structures can be understood from laser-matter interaction. Many researchers the reported the synthesis of nanostructures employing laser ablation in liquid ambient. The morphological changes that occurred during laser ablation is greatly affected by ablation time. However, it is difficult to observed the morphological changes of In_2Se_3 nano-cube transformation (from SEM and UV analysis). Hence, in order to understand the exact role of ablation time, we have prepared the samples with different ablation time varies from 5 to 60 minutes. It is found that In_2Se_3 bulk sheets were totally transformed into In_2Se_3 nano-cubes after 20 minutes. The SEM images in figure 9 clearly show that the ablation time is one of the important parameters in the transformation process of In_2Se_3 nano-cubes. Therefore, major role of ablation time is to reduce the particle size from bulk In_2Se_3 micro sheet into spherical In_2Se_3 nano-cubes. It is reported that decreasing particle size increases the surface energy which leads to decreasing stability of atoms in spherical nanoparticles[37]. Therefore, atoms in a spherical nanoparticle can move in the same nanoparticle. This continuous movement of atoms can be responsible for the formation of stable morphology in

the form of nano-cube with facet[86, 87]. This shows that laser ablation conducted at the different time help to supports the movement of free atoms and enhance the transformation process. Besides this, the role of solvent (water) is to stabilize the surfaces of nano-cubes which causes an increase in In_2Se_3 nano-cubes transformation. Understanding the transformation process, laser ablation time and water are the key factors in transforming the morphological changes from bulk sheets in to nano-cubes.

3.4 EDS and XPS analysis

To check stoichiometry and chemical composition we observed the samples in SEM attached energy-dispersive X-ray spectroscopy (EDS), as shown in figure 12. Figures 12A and 12B show EDS spectra of bulk and laser ablated samples, respectively, which provides the elemental

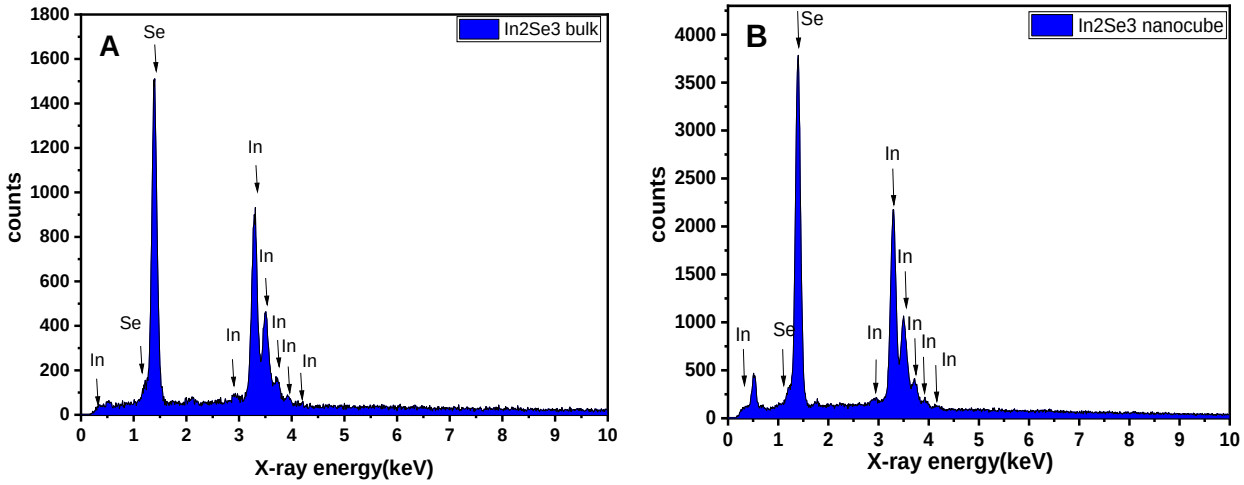

Figure 12: EDS analysis of In_2Se_3 bulk and nanocubes

composition of indium and selenium. From these data, it is confirmed that there is no change in the stoichiometry of In_2Se_3 after ablation.

The chemical composition and valence state of bulk and laser-ablated In_2Se_3 were examined by the XPS instrument. The full scanned spectrum of bulk and the laser-ablated In_2Se_3 is shown in figure 13A and 13D**,** which shows the presence of elements In, Se, C, O in the sample. The C1s peak observed at the binding energy of 284.6 eV was considered as a reference to calibrate the

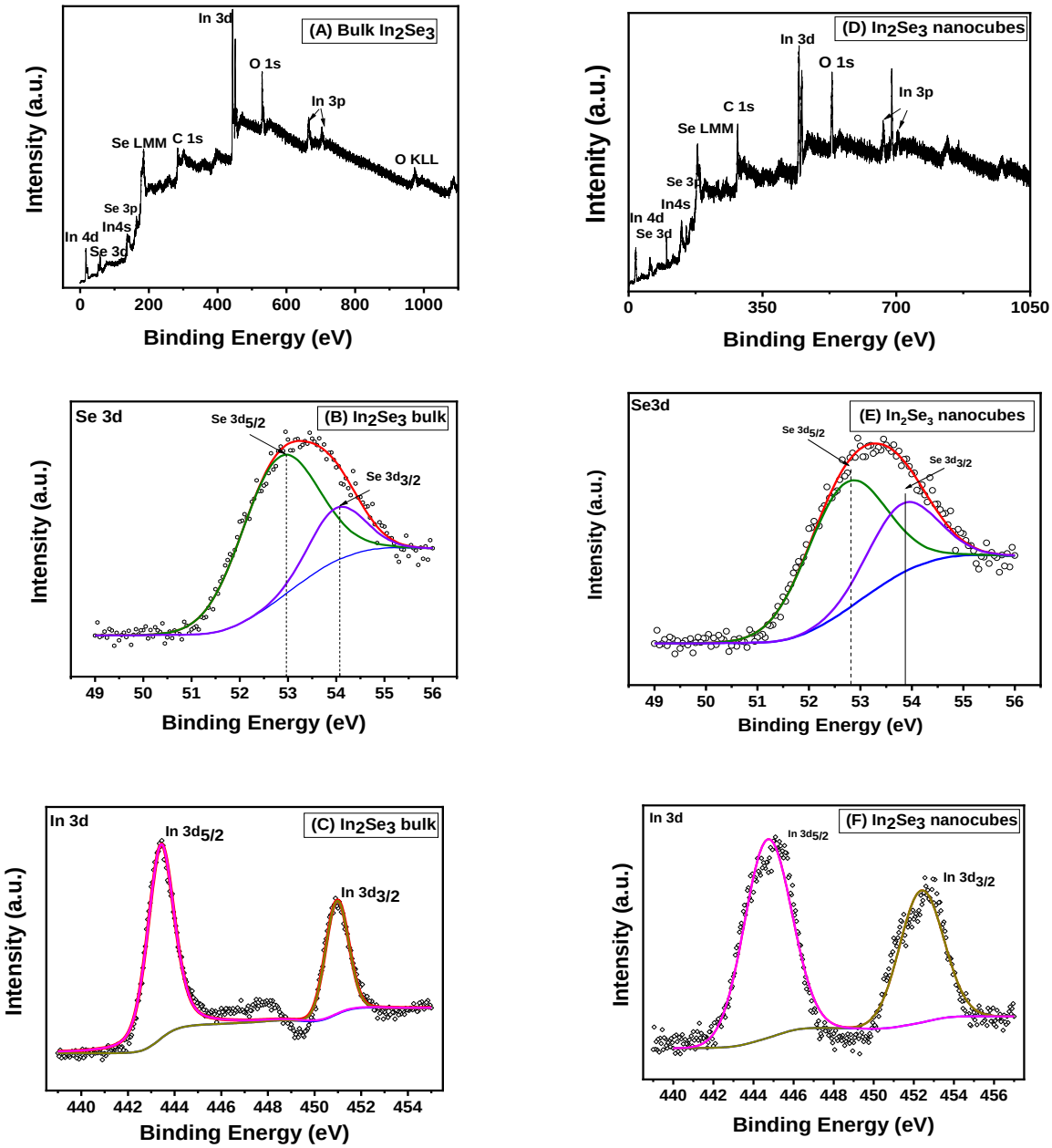

Figure 13: (A) Full-scale XPS spectra of bulk In_2Se_3 (B) Se 3d doublet peak of bulk In_2Se_3 (C) In 3d subshell energy of bulk In_2Se_3 (D) full-scale XPS spectra of In_2Se_3 nano-cubes (E) Se 3d doublet peak of bulk In_2Se_3 (F) In 3d subshell energy peak of bulk In_2Se_3 nano-cubes.

observed binding energies. The carbon peak appears at 284.6 eV as allocated to foreign carbon based adulterate, which is used to calibrate all of the binding energy of the samples, whereas the oxygen element peak appears feasibly due to absorption of oxygen molecular species on the surface of both samples. The XPS spectra of the bulk and the laser-ablated In_2Se_3 are likewise to the typical In_2Se_3 spectrum reported in the literature[88, 89].

The de-convoluted XPS spectrum of In3d (figures 13 (B) and (C)) illustrates two characteristic peaks at binding energies of 443.5, and 451.0 eV, corresponding to In $3d_{5/2}$ and $3d_{3/2}$, with a difference of 7.5 eV, which is consistent with standard Indium. According to a previous study, the In 3d peaks are often broaden in compounds, with respect to pristine metal. Furthermore, this phenomenon may be a general characteristic of an indium chalcogenide with defect nature[90, 91]. In the present study, the full width half maximum (FWHM) of the In $3d_{5/2}$ and $3d_{3/2}$ peaks in nano-cubes sample is more as compared to the bulk sample, and may be attributed to the O 1s signal, which coincides with a small shoulder in the In 3d region with In 3d5/2 peak at 444.8 eV.

The O 1s signal likely is due to residual oxygen species contamination as physiosorbed (molecular) species, although the formation of oxide phase on the surface cannot be ruled out during laser treatment. The two intense peaks observed at ~ 53.0 and 54.1 eV in the de-convoluted spectrum of Se3d level are attributed to the binding energy of Se 3d5/2 and Se 3d3/2, respectively.

3.5 Femtosecond Transient Absorption Spectroscopic analysis

UTAS data and the carrier dynamic proposed were shown in figure 14. Figure 14A shows the normalized transient absorption decay profiles of the photo-generated carriers in the bulk and nano-cube In_2Se_3 under the different excitation intensities. The absorption decay is mainly caused by electron-hole recombination. In the case of bulk In_2Se_3 (indicated as In_2Se_3As), the initial

recombination of electron-hole is faster but the recombination rate from 10 ps onwards is slower, whereas the indium selenide nano-cubes (indicated as In_2Se_3Ab) shows gradual electron-hole recombination throughout the observed time scale up to 500 ps. The observed similar decay profiles between different excitation intensities indicated that the carrier density is low enough to avoid the occurrence of 2nd order electron-hole recombination. Figure 14B shows the transient absorption spectra of the bulk and nano-cube In_2Se_3. The spectra of the bulk sample taken at 2 ps is broad and there is no sign of peak indicating free carriers are observed, whereas the spectra at

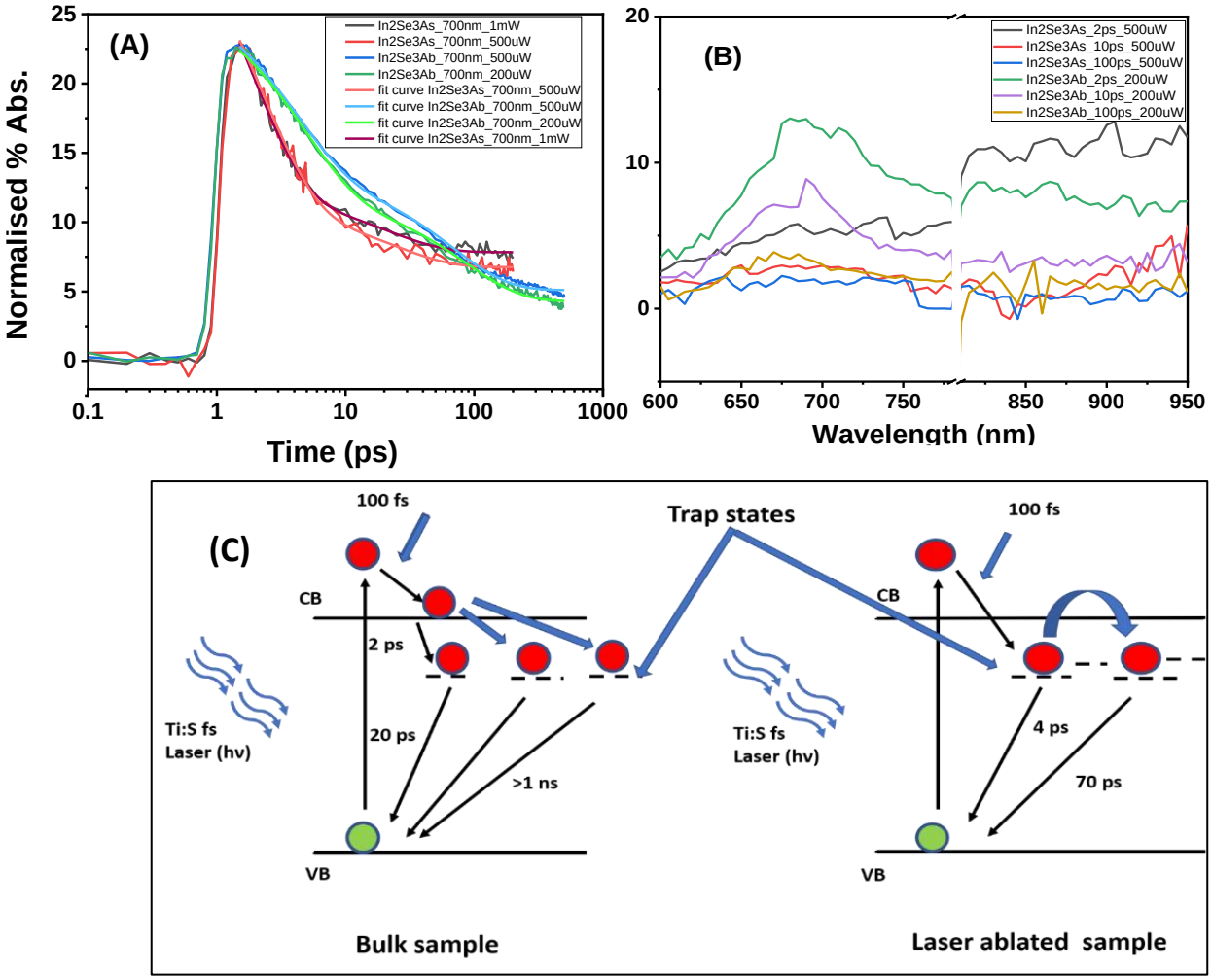

Figure 14: (A) Transient absorption spectra of bulk and In_2Se_3 nano-cubes (B) the optical density of the bulk and In_2Se_3 nano-cubes (C) schematic diagram of the behavior of an electron in bulk and In_2Se_3 nano-cubes.

10 ps and 100 ps give a broad peak around 670 nm showing carrier trapping. In the laser-ablated sample, the spectra at 2 ps, 10 ps, and 100 ps show a relatively sharp peak around 670 nm which suggests that the density of trap states in the ablated sample is more than the bulk sample so that free carriers have been trapped within ~1 ps. With the reference to both transient absorption profiles and spectra, using the help of double-exponential decay fitting. we suggest a model (figure 14C) in which we give an illustration of charge carrier dynamics in bulk and laser-ablated In_2Se_3. In the model of the bulk sample, the decay of the charge carriers shows two-level decay. In the first level, charge carriers' decay to trapped states in 2 ps, and the second level decay, they recombine with holes in the valence band. After 20 ps, onwards the decay gets slower as it survives >1 ns. It suggests that the charge carriers are traveling among the trapped states in the bulk sample. The electron that moved far away recombine with the hole very slowly. Laser-ablated sample also shows the two-level decay process but having different decay process. In the laser-ablated sample, the charge carriers are decaying slower than the bulk material until ~50 ps. As we stated earlier that the number of trapped states of an ablated sample is more than that in the bulk sample; therefore, free electrons are trapped quickly. Because of the multi-trapped states, charge carriers cannot move far away from holes. The first decay of the trapped electrons took 4 ps and then slowly decays to the valance band to recombine with holes. According to a common peak position (670 nm) between bulk and nano-cubes, there are no deep trap levels present even in the nano-cubes. Electrons in nano-cubes, therefore, can be regarded as mobile carriers through the hopping process and thus travel over long distances in the absence of holes. In this case, the morphology plays a major role in field electron emission. The cubical indium selenide has sharp edges and corners which help higher electron ejection. This mechanism shows that the smaller the particle

size the more charge carriers can jump to the conduction band with sufficient time to get out of the surface of the material after applying sufficient voltage which matches with FE studies (figure 15).

3.6 Field electron emission analysis

The FE current density (J) versus applied electric field (E) characteristic of In_2Se_3 nano-cubes emitter is shown in figure 15A. From the J-E curve, the value of the turn-on field, defined at

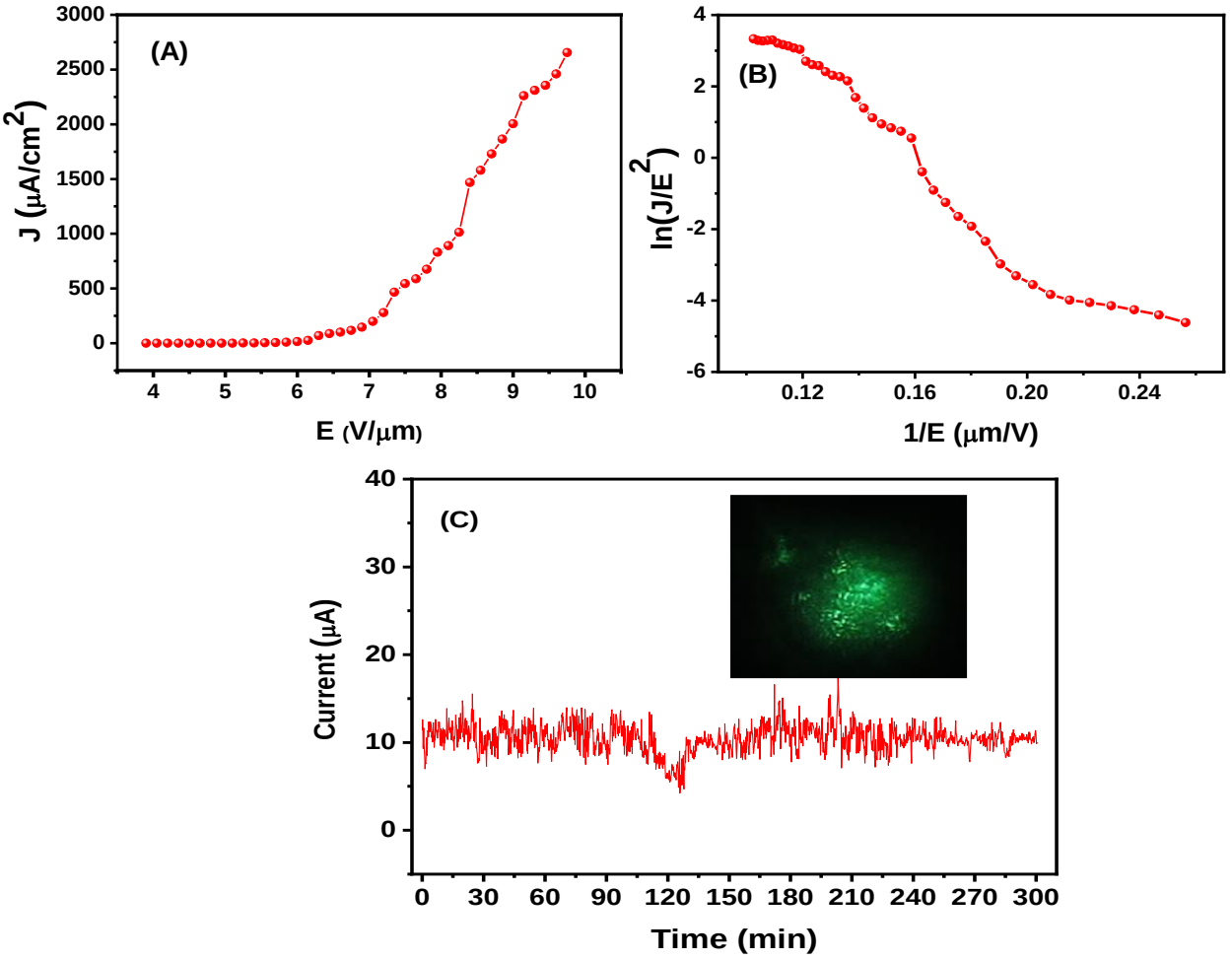

Figure 15: Field emission characteristics of In_2Se_3 nano-cubes planar emitter (A) emission current density versus applied electric field (J-E) plot, (B) Fowler-Northeim plot, and (C) emission current versus-time (I-t) plot of nano-cubes. The inset in fig. (C) shows a typical field emission image photographed at the onset of the stability measurement

emission current of density of ~ 10 μA/cm^2 is found to be ~ 5.8 V/μm, and the threshold field, defined at emission current of the density of ~ 100 μA/cm^2, is found to be ~ 6.5 V/μm. The exponential nature of the J-E curve implies that the emission is as per the Fowler-Northeim (F-N) theory of field emission[71]. With a further increase in the applied field, a maximum emission current density of ~ 2656 μA/cm^2 is extracted at an applied field of ~ 9.7 V/μm. In the present study, the applied electric field (also referred to as an average electric field) is defined as E = V / d, where V is the applied voltage and d is the separation between anode and cathode. Similarly, the emission current density J is defined as J = I / A, where I is the experimentally measured emission current and A is the total area of the emitter (~ 25 mm^2). The values of the threshold field and maximum emission current density extracted with corresponding field value are superior to those reported for field emitters due to In_2Se_3 nanostructures[66, 69, 70]. The well facetted nano-cubes, owing to their nanometric dimensions, possess protrusions, which are responsible for significant enhancement in the local electric field. The sharp edges and corners of these nano-cubes act as potential emission sites. Furthermore, the random orientation of these nano-cubes noticeably minimizes the field screening effect. Thus, the moderate areal density, random orientation, and minimum field screening effect, availability of numerous potential emission sites, and maintained electrical properties (revealed from UTAS analysis makes the In_2Se_3 nano-cube emitter competent to deliver very large emission current at relatively moderate applied field. Furthermore, we have measured the FE performance of pristine carbon tape (without In_2Se_3 nanocubes), which exhibits field emission in very high field region. As they do not have any sharp structure, they do not affect the FE performance of In_2Se_3 nanocubes emitter. The obtained turn-on value of In_2Se_3 nano-cubes is considerably lower than reported nanostructures whereas maximum current density is found to be higher as compared with various emitter materials.

The observed J-E characteristic is further analyzed by plotting a graph of $ln\ (J/E^2)$ versus $(1/E)$, known as F-N plot. The F-N plot, depicted in Figure 15(B), exhibits deviation from linear nature with tendency towards saturation in the high field region. The deviation from linearity is attributed to the semiconducting nature of the emitter. Furthermore, for a planar emitter (comprised of nanostructures deposited in thin film form on a suitable substrate), various factors including, variation in the aspect ratio of the nanostructures, field penetration and screening effect, band bending, etc. are responsible for non-linear nature of the F-N plot[92].

Furthermore, emission current stability, one of the important parameters defining the performance of an emitter, has been tested at pre-set value of 10 μA over the duration of 5 hours. From figure15(C)

the emission is observed to be fairly stable, characterized by 'spike' like fluctuations superimposed on the base current, along with very few excursions. The spike like fluctuations is due to various atomic scale processes such as, adsorption, desorption, and/or migration of residual gaseous species on the emitter surface. The observations of excursions in emission current can be attributed to the 'extinction' and 'regeneration' of the emission sites. In a planar emitter, when emission is on, the *in-situ* bombardment of residual ionic species on the emitter surface results into sputtering, which may noticeably change the aspect ratio of the nanostructures thereby making them either a potential emission site (regeneration of site) or stopping emission from the existing site (extinction of site). Overall, the In_2Se_3 nano-cubes emitter exhibits good emission current stability, characterized with a standard deviation of 3.17.

Chapter 4: Photocatalytic activity of In_2Se_3 and its nanocomposite

4.1 SEM, TEM and HRTEM analysis

The FESEM and TEM images of In_2Se_3 composite collected after laser ablation is shown in Figure 16. Figures 16A, 16C, and 16E show the SEM images of In_2Se_3 nanocubes, whereas Figures 16B, 16D, and 16F show the TEM images of In_2Se_3 nanocubes, In_2Se_3/Au, and In_2Se_3/ZnO/Au respectively with HRTEM images in the inset. The surface morphology of the In_2Se_3 laser-ablated in the DI water (Figure 16A) is identified as nanocubes with a regular shape having an average size ~68 nm and the corresponding TEM image (Figure 16B) shows even color contrast which suggests the improvement in particle defect and having even surface, as well as the inset of high-resolution transmission electron microscopic image shows lattice spacing of ~0.33 nm corresponds to the (100) crystalline plane of In_2Se_3. Figures 16C and 16D depict SEM and TEM images of In_2Se_3 well-faceted nanocubes decorated with AuNP having ~7 nm average particle size. The inset of figure D shows HRTEM images with the lattice spacing of ~0.33 nm and 0.22 nm corresponds to the crystal plane (100) and (111) of In_2Se_3 and AuNP respectively. Figures 14E and 14F show SEM and TEM of the crystalline sheets of In_2Se_3 and ZnO decorated with AuNP. The average particle sizes AuNP is ~5 nm deposited on sheets of In_2Se_3 and ZnO which shows the substantial change in the morphology as we introduce the hydrothermal reactor into the synthesis process. The TEM and SEM images show all materials are well attached to each other and make a well-bound composite for charge transfer. Inset images of HRTEM show lattice spacing 0.33 nm, 0.25 nm, 0.22 nm corresponds to In_2Se_3, ZnO, and AuNP.

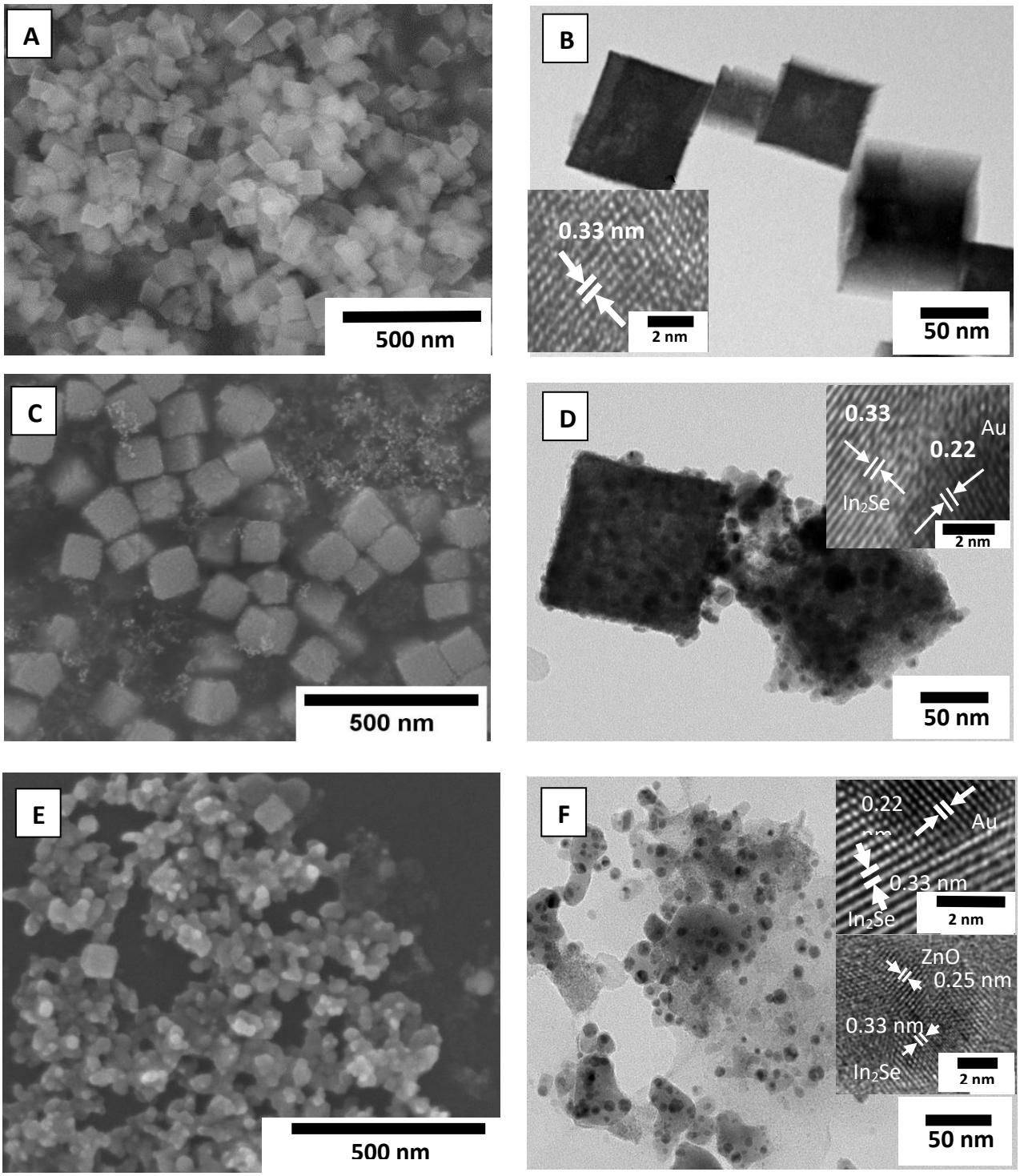

Figure 16: SEM, TEM and HRTEM images of In_2Se_3 and its composite(A) SEM image of In_2Se_3 nanocubes, (B) TEM image of In_2Se_3 nanocubes with HRTEM image in inset(C) SEM image of In_2Se_3 decorated with Au, (D) TEM image of In_2Se_3 decorated with Au with HETEM images in inset, (E) SEM image of In_2Se_3/ZnO decorated with AuNP, and (F) TEM image of In_2Se_3/ZnO decorated with AuNP with HRTEM image in inset

4.2 EDS analysis

To examine chemical constituents in the respective samples, we have analyzed the samples using energy dispersive X-ray electron spectroscopy (EDS) as shown in Figure 17. The samples were observed on the carbon tape, so the spectra also exhibit the peak of C. Figures 17A, 17B, 17C, and 17D show the presence of In, Se, Au, O, and Zn which shows the composite made correctly. From

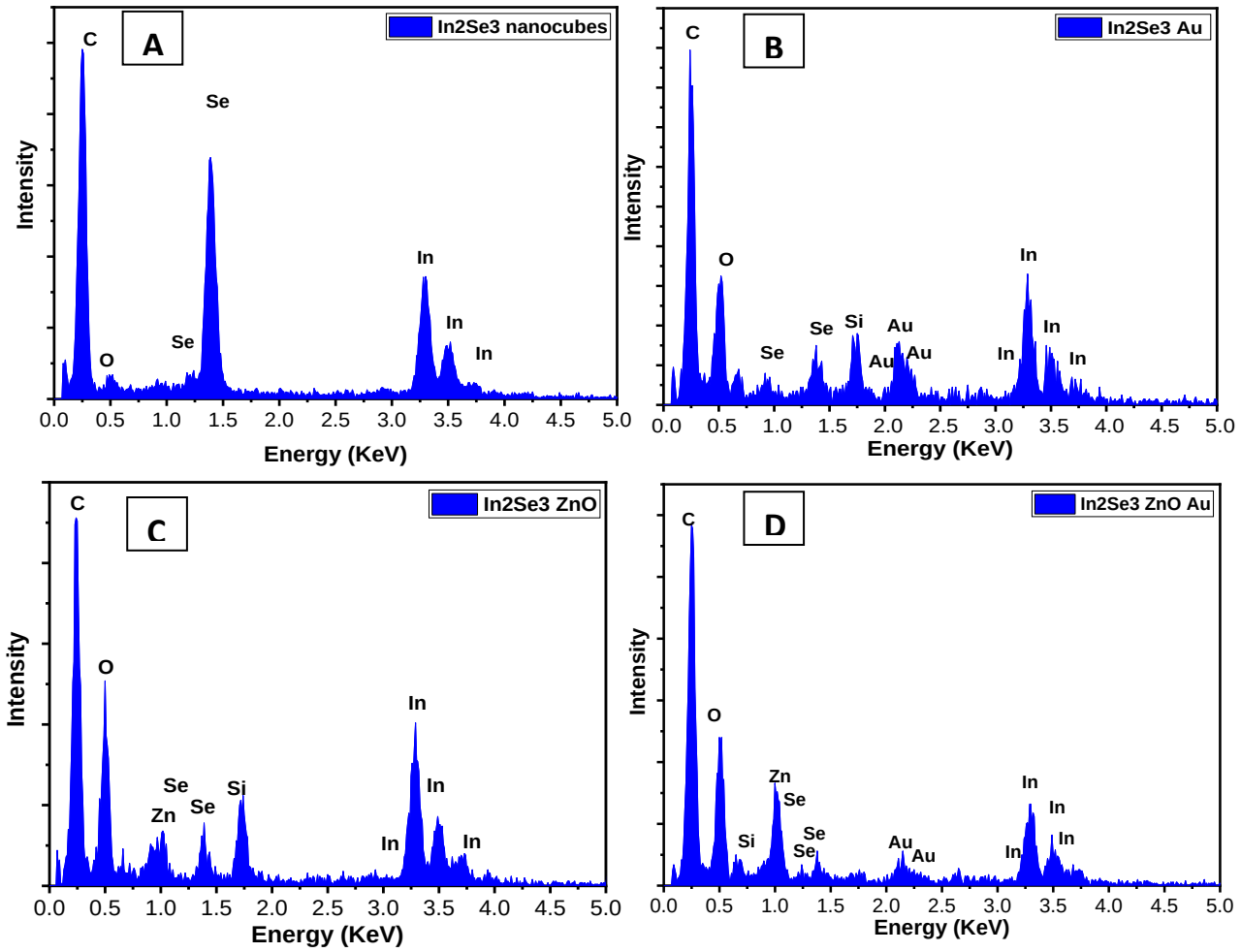

Figure 17: (A) SEM-EDS spectra of In_2Se_3 nanocubes, (B) In_2Se_3/Au, (C) In_2Se_3/ZnO, and (D) In_2Se_3/ZnO/Au composite

these data, it confirms that even after laser ablation and hydrothermal process the stoichiometry of In_2Se_3, ZnO, and Au did not change.

4.3 Micro Raman analysis

To examine the structural properties of In_2Se_3 nanocubes and its composite with ZnO and AuNP, we have performed the micro-Raman analysis. Figure 18 described the corresponding Raman spectra taken at ambient temperature. A cautious observation of Raman spectra reveals that the corresponding peak at 107 cm^{-1} belongs to the transverse optical (TO) + longitudinal optical

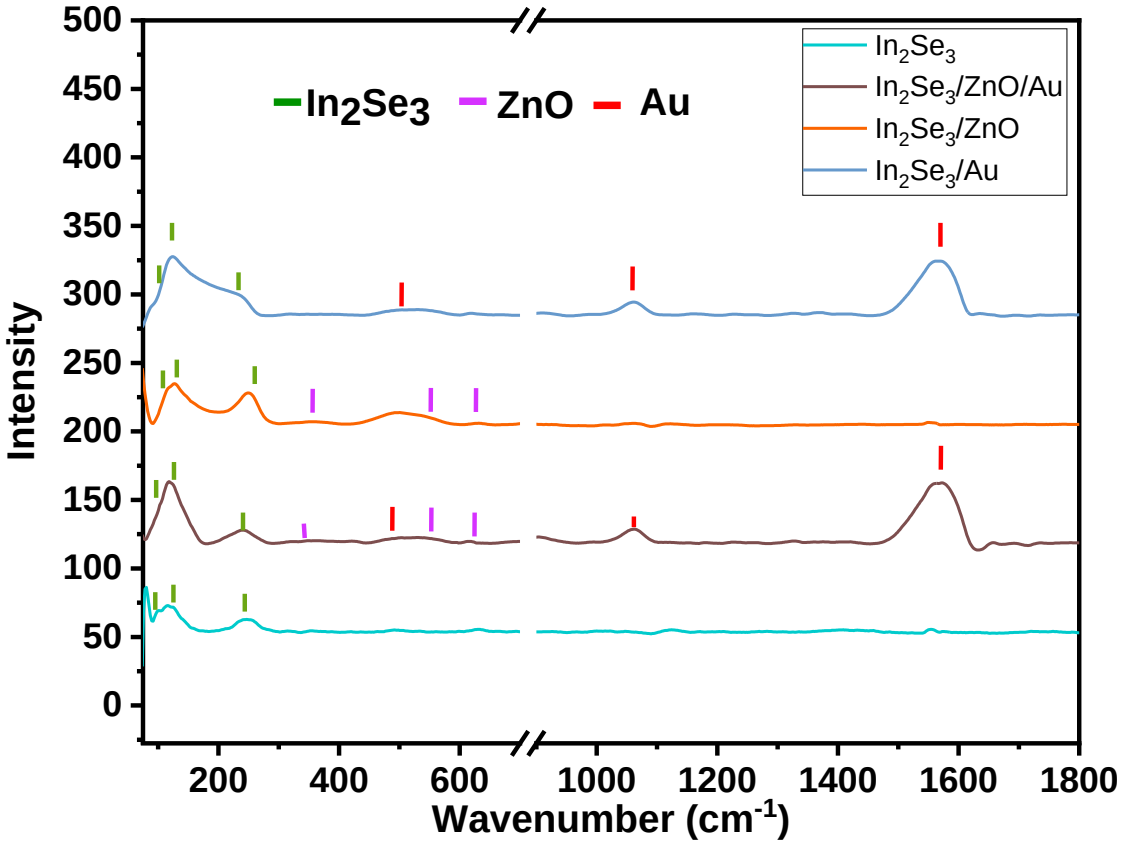

Figure 18: Raman spectra of In_2Se_3, In_2Se_3/Au, In_2Se_3/ZnO, and In_2Se_3/ZnO/Au

(LO) modes of In_2Se_3, whereas 130 cm^{-1} and 250 cm^{-1} belongs to TO mode and LO mode of In_2Se_3 respectively[85]. In_2Se_3/ZnO, the TO mode shifted towards higher wavenumber due to the presence of a small amount of oxygen in the material. The peaks ~236 cm^{-1}, ~570 cm^{-1}, and ~620 cm^{-1} correspond to the optical modes of ZnO. These peaks are broad due to surrounding chemical compounds and less crystallinity of ZnO as well less amount (~10%) of ZnO present in the

sample[93, 94]. AuNP decorated samples show the peaks of AuNP at ~490 cm^{-1}, ~1080 cm^{-1} and ~1560 cm^{-1}.

4.4 UV-Vis spectroscopy analysis

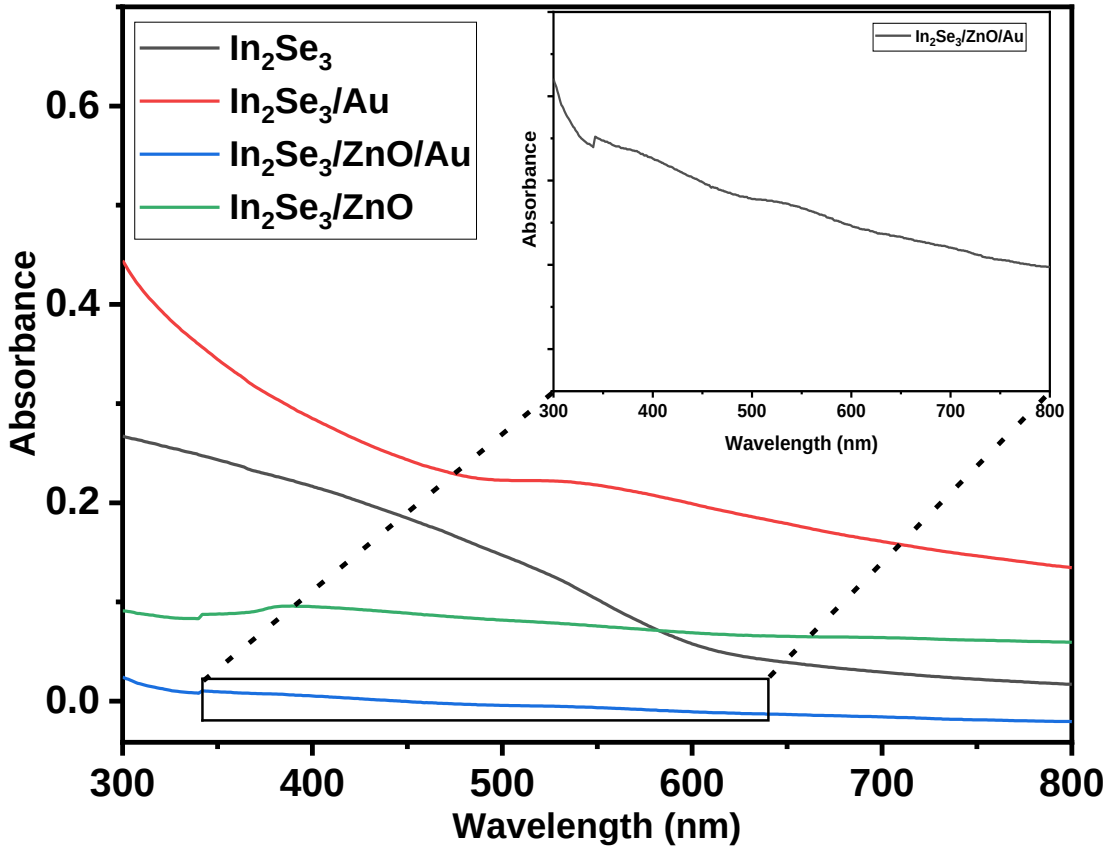

Figure 19: UV-Vis spectra of In_2Se_3 nanocubes, In_2Se_3/Au, In_2Se_3/ZnO, in_2Se_3/ZnO/Au with a zoomed image of In_2Se_3/ZnO/Au in the inset.

The absorbance properties of prepared composites were measured by UV-Vis spectroscopy. Figure 19 illustrates the UV-Vis spectra of In_2Se_3 nanocubes, In_2Se_3/Au, In_2Se_3/ZnO, and In_2Se_3/ZnO/Au. It can be seen from the spectra that In_3Se_3/Au and In_2Se_3/ZnO/Au (inset image of Figure 5) show absorption around 520 nm, which is associated with the plasmon absorption band of AuNP. In_2Se_3/ZnO and In_2Se_3/ZnO/Au spectra of Figure 19 show a broad peak around 380 nm which suggests that the bandgap energy is ~3.2 eV[34]. The calculated bandgap energy is lower than the

bulk ZnO, this decrement in the bandgap can be due to the quantum confinement effect and presence of intrinsic crystal defects caused by laser ablation[53, 95].

4.5 Femtosecond Transient Absorption Spectroscopic analysis

Prepared catalysts were examined by the femtosecond ultrafast transient absorption spectroscopy as shown in Figure 20. Figure 20 A shows the transient absorption spectra of In_2Se_3 nanocubes measured at -1.5 ps, 0 ps, 10 ps, 50 ps, 100 ps, and an average of 500 ps to 1000 ps. The bleach was observed from 400 nm to 580 nm which is due to the excitation of electrons from the valance band to the conduction band in In_2Se_3, and the density of charges gets an increase in the conduction band. The optical density from 580 nm and above reveals the electrons are trapped in trap states, particularly with a peak around 620 nm which shows the highest absorbance even above 100 ps, suggesting that the electron mobility is less in nanocubes after electron trapped in a trapped state. In our previous study, mobile electrons in bulk In_2Se_3 were observed in the NIR region and electron trapping caused spectral blue-shift, giving a peak at 620 nm[83]. Optical density at -1.5 ps, 0 ps, 10 ps, 50 ps, 100 ps, and an average of 500 ps to 1000 ps of In_2Se_3/Au shows in figure 20 B, which shows the absorption form 400 nm to 550 nm corresponding to the absorption of AuNP nanoparticle which cancels the bleaching effect In_2Se_3 nanocubes. Also, NIR broad absorption is seen at 0 ps. This suggests that the pump laser at 400 nm mainly excites AuNP and the transfer of electron occurs from AuNP to In_2Se_3 nanocubes within the time resolution. The absorption from 550 nm to 1150 nm decays with time, suggesting that the trap states are not active so electrons in In_2Se_3 can transfer backward and recombine faster with holes in AuNP. Optical absorption spectra of In_2Se_3/ZnO/Au are shown in figure 20 C which is taken at -1.5 ps, 0 ps, 10 ps, 50 ps, 100 ps and

an average of 500 ps to 1000 ps. With respect to time, the absorption of 400 nm to 550 nm region constantly decreases, whereas that of 550 nm to 700 nm region maintains the absorption with corresponds to the In_2Se_3, and also maintains absorption till 1050 nm. By closely observing the

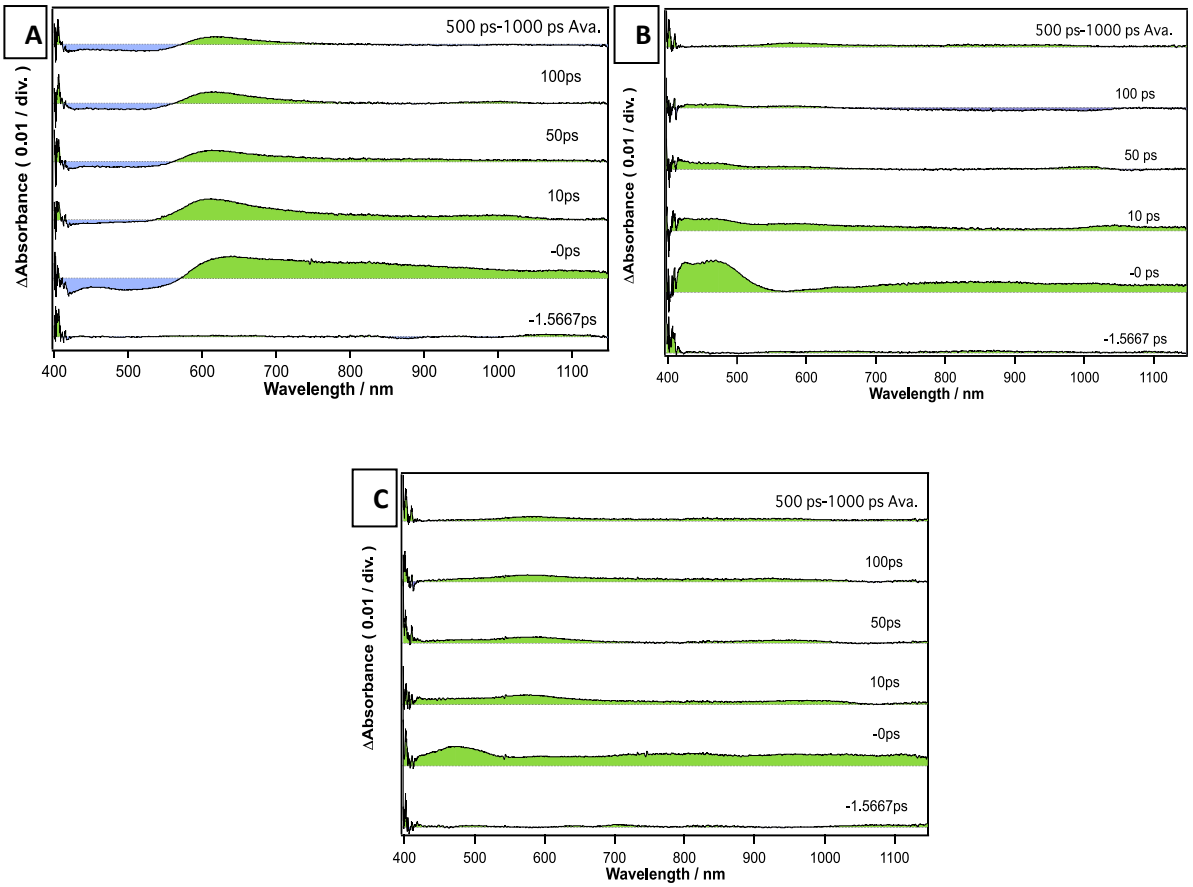

Figure 20: Optical density of composites taken after laser irradiation (A) In_2Se_3 nanocubes, (B) In_2Se_3 decorated with AuNP, and (C) In_2Se_3 /ZnO decorated with Au

structure of In_2Se_3/ZnO/Au (TEM image in Figure 16 F), electrons are seeming to transfer from AuNP to either In_2Se_3 or ZnO or both of them. To verify the charge transfer mechanism, we have checked the decay profiles (Figure 21) at 620 nm (Figure 21A) which corresponds to trap state electron decay and those at 900 nm (Figure 21 B) which corresponds to the mobile electron present in the catalyst system. The decay profile is normalized at In_2Se_3 nanocubes peak and fitted using a triple exponential X offset curve as shown in equation 1. The decay profile at 620 nm shows the

$$f(t) = A_1 * exp\ (-(t-X_0)/\tau_1) + A_2 * exp\ (-(t-X_0)/\tau_2) + A_3 * exp\ (-(t-X_0)/\tau_3) + Y_0 \quad (1)$$

~4 ps rising approach in In_2Se_3/Au attributed to plasmon bleaching recovery (electron-phonon scattering) and a certain number of electrons transferred from AuNP to In_2Se_3 nanocubes system, while the decay approach of the In_2Se_3/Au system shows the pronounced recombination of charges. Both In_2Se_3/ZnO/Au system and In_2Se_3 nanocubes systems show a similar ~3 ps rising approach

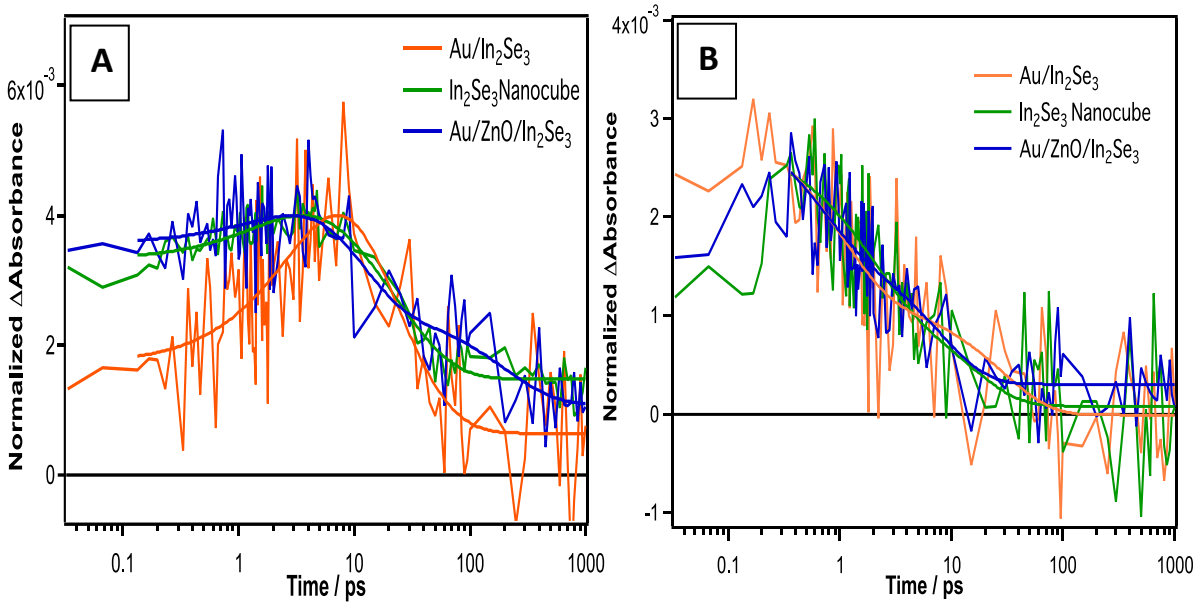

Figure 21: Time profile spectra of In_2Se_3, ZnO and AuNP composites (A) decay spectra taken at 620 nm and (B) decay spectra taken at 900 nm

and slow decay rate than In_2Se_3/Au system. Whereas the decay approach of the In_2Se_3/ZnO/Au system is slightly different than that of the In_2Se_3 nanocubes system. The In_2Se_3/ZnO /Au system shows a slower decay rate from 20 ps to 300 ps which indicates that the charges are separated and recombination is slower than that of others. To check the involvement of mobile charge carriers in the catalytic system, we took decay profiles at 900 nm as shown in Figure 21 B. The profiles were normalized and fitted using double exponential X offset as shown in equation 2. The profiles

$$f(t) = A_1 * \exp(-(t-X_0)/\tau_1) + A_2 * \exp(-(t-X_0)/\tau_2) + Y_0 \quad (2)$$

distinctly show the charge transfer from AuNP to In_2Se_3 and/or ZnO inducing the lifetime change in the In_2Se_3/ZnO/Au system to be longer than the other two systems, as indicated by the clear presence of signals after 100 ps.

Figure 21 A and 21 B confirms that the charge separation in In_2Se_3/ZnO/AuNP system is better than In_2Se_3 nanocubes and In_2Se_3/Au system. The fitting parameter of graphs 21 A and 21 B are shown in table 1 and table 2.

Table 1 3. Exponential (triple) decay times at 620 nm of photocatalytic systems

	t_1 (ps)	**t_2 (ps)**	**t_3 (ps)**
In_2Se_3 Nanocubes	2.05 ± 1.10	16.0 ± 55.3	35.4 ± 76.3
In_2Se_3 /Au	3.91 ± 5.11	15.0 ± 121	36.5 ± 201
In_2Se_3/ZnO/ Au	2.53 ± 3.85	9.29 ± 11.9	201 ± 170

Table 2. Exponential (double) decay at 900 nm of the photocatalytic system

	t_1 (ps)	**t_2 (ps)**
In_2Se_3 Nanocubes	1.78 ± 1.29	14.7 ± 14.3
In_2Se_3 /Au	1.03 ± 0.487	28.7 ± 16.5
In_2Se_3/ZnO/Au	0.610 ± 0.506	7.64 ± 3.59

4.6 Reduction of Methylene Blue and Efficiency of photocatalytic reduction

For the concrete evidence, we have examined the In_2Se_3 nanocubes system, In_2Se_3/ZnO, and In_2Se_3/ZnO /Au system using photodegradation of organic dye method. For this method, we choose methylene blue dye, and the results are shown in Figure 22. As methylene blue absorbs visible light with two characteristic peaks at 612 nm and 665 nm and after reduction it became

colorless, the photocatalytic reduction can be monitored using the spectrometric method. The photogenerated electrons in the catalyst are further involved in the reduction of methylene blue. In

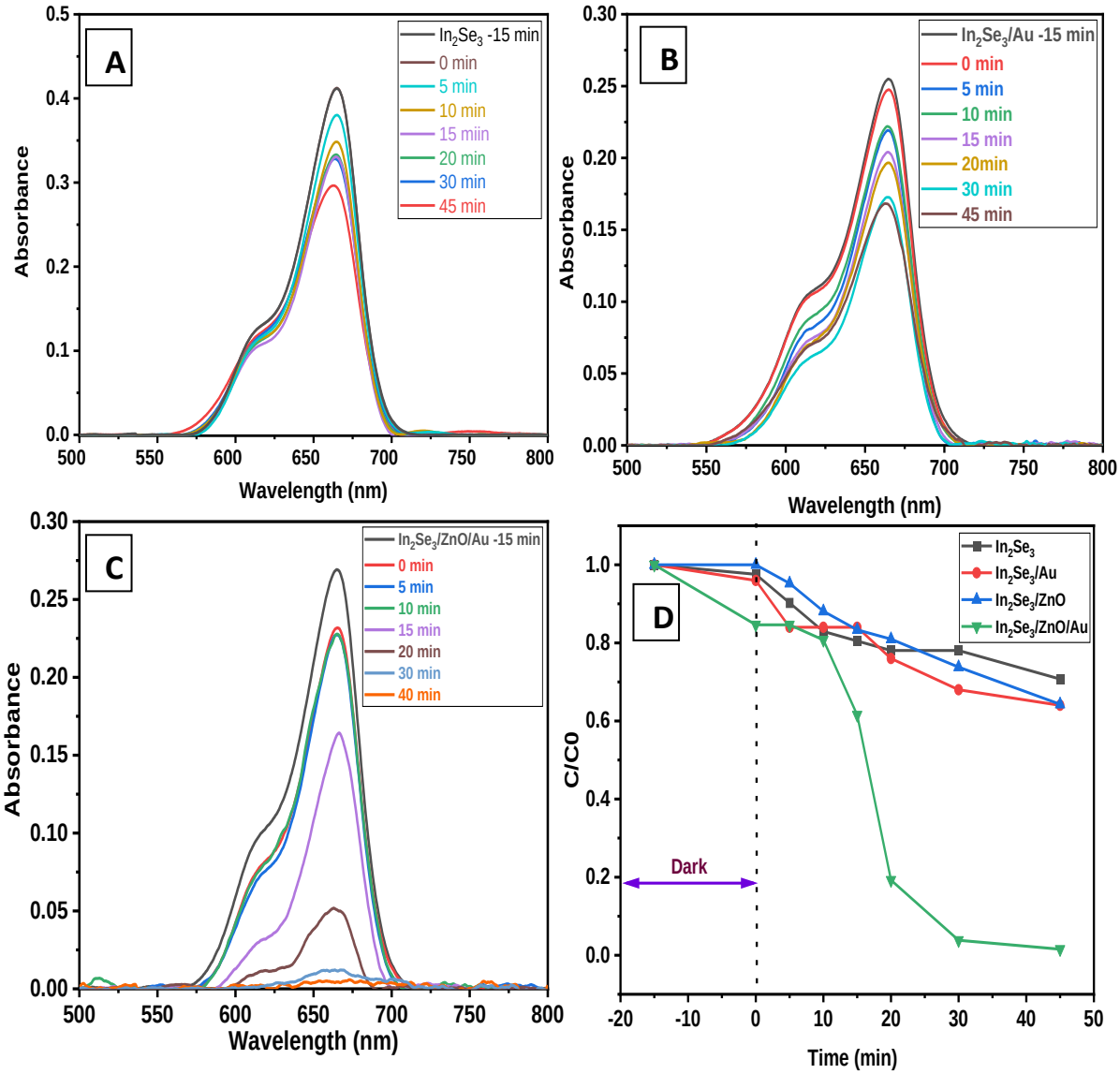

Figure 22: Photocatalytic reduction of MB using (A) In_2Se_3 nanocubes catalyst (B) In_2Se_3/Au catalyst (C) In_2Se_3/ZnO/Au catalyst and (D) photocatalytic degradation efficiency of photocatalytic system

Figure 20 C for In_2Se_3/ZnO/Au, it can be seen that the absorption characteristics decrease quickly under visible light irradiation than In_2Se_3 nanocubes (Figure 22 A) and In_2Se_3/Au (Figure 22 B). 45 minutes of illumination on In_2Se_3/ZnO/Au system shows 100% degradation whereas In_2Se_3 nanocubes system, In_2Se_3 /Au and In_2Se_3/ZnO shows 27%, 32% and 32% respectively. It should

be noted that the optical absorption of In_2Se_3/ZnO/Au is the lowest among all catalysts investigated (see Figure 19). Figure 22 D shows the comparative efficiency, in which only In_2Se_3/ZnO/Au system shows the higher adsorption among all systems as indicated by the signal drop before irradiation. Because of having sheet morphology more surface area is available to adsorb MB. Spectra also indicates that the catalytic system is primarily having less diminution till 10 minutes and then diminishes at a higher rate. Moderated diminution is caused by the incompletion of electron transfer to the adsorbed MB molecules. Once the primary process is completed, electron transfer to methylene blue gets faster for reduction. The photodegradation of MB using In_2Se_3/ZnO/Au matches with the UTAS spectra of In_2Se_3/ZnO/Au which shows the charge transfer and well charge separation. Based on both UTAS and photocatalysis, we concluded that there might be two possibilities of charge transfer mechanism as illustrated in Figure 23. Figure 23 gives a direct understanding of a systematic process of photocatalysis Figure 23 shows that in the photocatalysis process AuNP and In_2Se_3 are simultaneously excited by the xenon light (without UV-light) and charge transfer occurs. Due to excitation, electrons are injected from AuNP to the conduction band of ZnO, because of its electron accepting nature from AuNP[96]. Injected electrons in the ZnO conduction band then move to In_2Se_3, and the electron rush present in the conduction band of In_2Se_3 gets transferred to the MB. There might be another possibility of a charge transfer mechanism, in which AuNP and In_2Se_3 were excited simultaneously. The electrons of AuNP transfer to In_2Se_3 and then transfer to the conduction band of ZnO. From Figure 20 D, the In_2Se_3/ZnO binary system did not show enhancement in photocatalytic activity compared with In_2Se_3 nanocubes. Therefore, the charge transfer from In_2Se_3 conduction band to ZnO conduction band is unlikely.

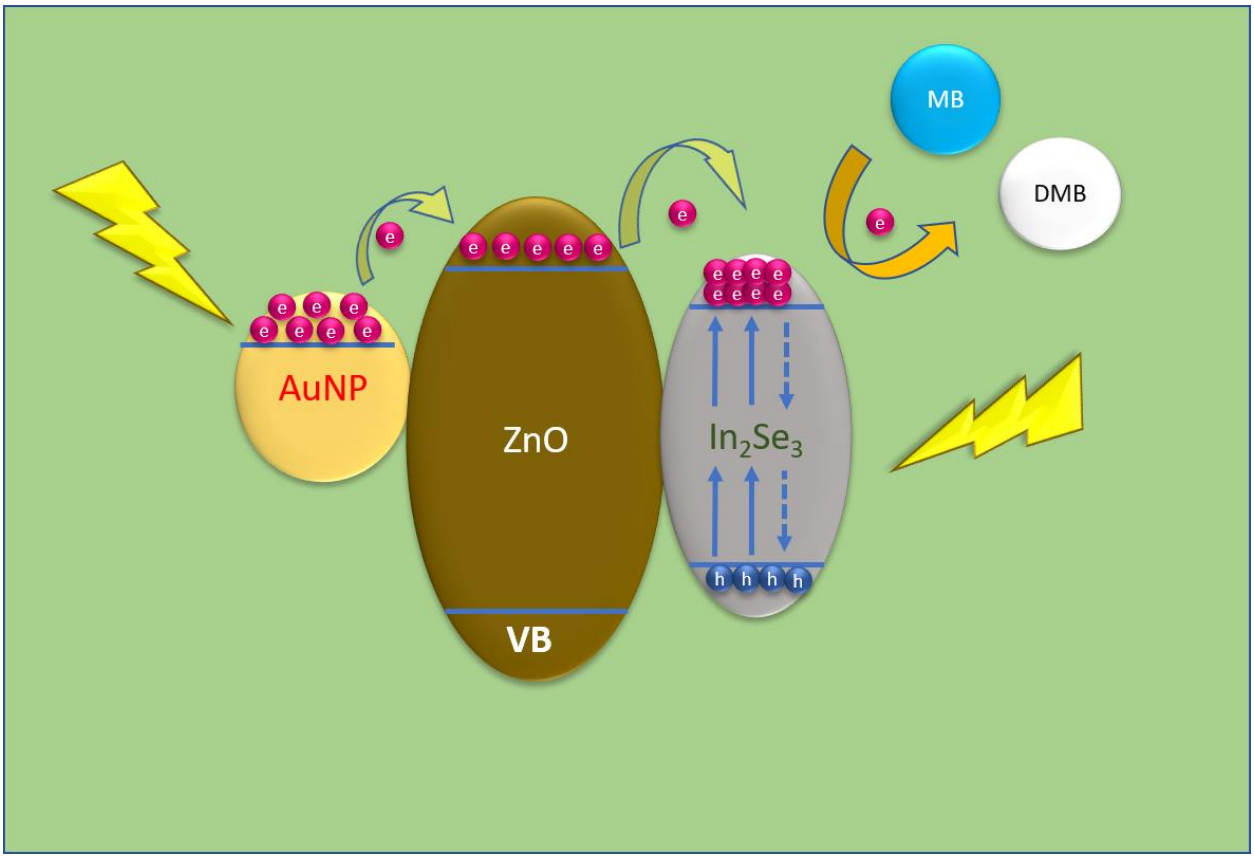

Figure 23: Graphical illustration of photocatalysis of the methylene blue (MB) by In_2Se_3/ZnO/Au. Degraded methylene blue (DMB)

Chapter 5: Production of Few layers Graphene from graphite by scanning UV laser

5.1 TEM and HRTEM analysis

Figure 24 depicts the TEM and HRTEM of the synthesized few layers graphene (FLG) using UV laser scanning on a graphite plate. Figure 24A shows TEM image of graphene produces by UV laser scanning on the graphite under water. The FLG sheets show the irregular in shapes with more than 10 sheets. Laser scanned under IPA (Figure 24 B) shows separated layers of graphene and

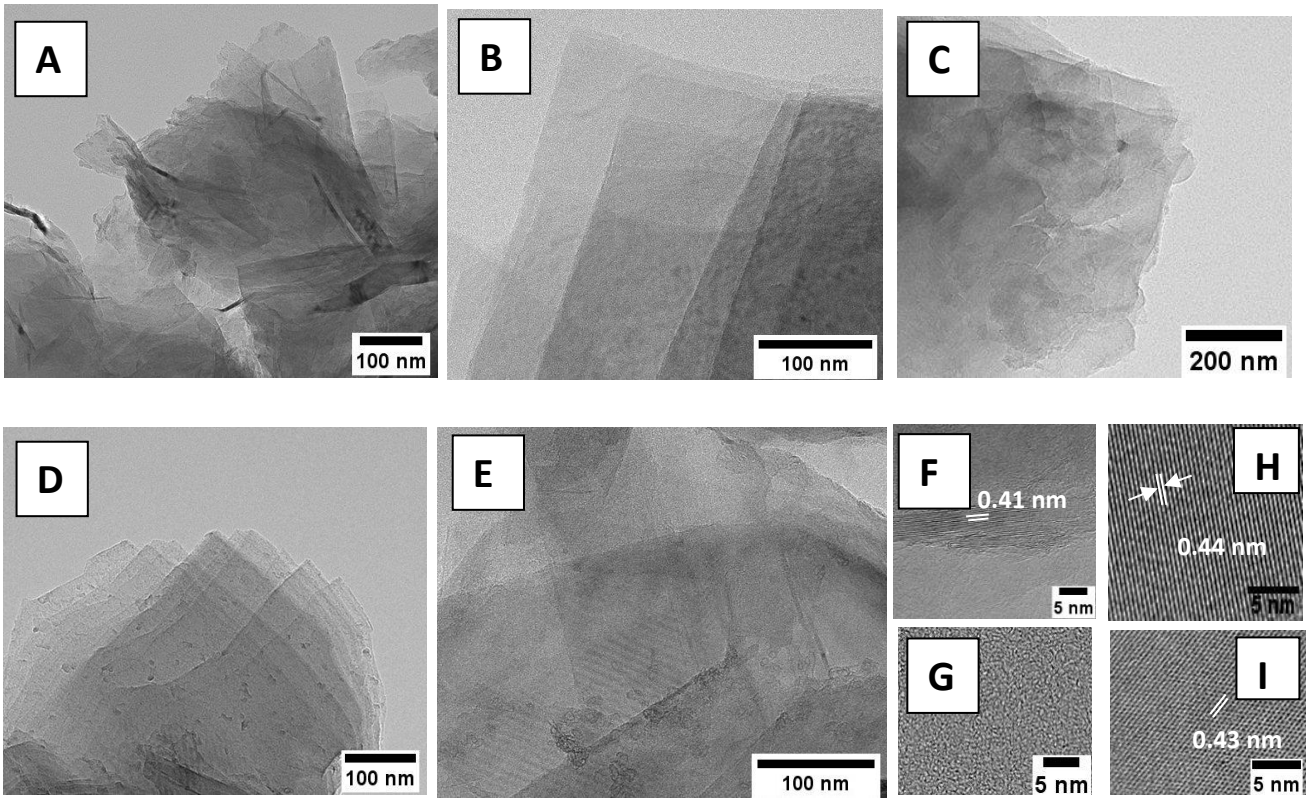

Figure 24: TEM (A) Water (B) IPA (C) Methanol (D) 50% Water and 50% Ethanol (E) Ethanol and HRTEM images (F) Methanol (G) Water (H) Ethanol (I) IPA of graphene synthesized using scanning UV laser ablation

undamaged surface or sheets whereas under scanned under ethanol (Figure 24 C) shows damaged graphene layers, which seems more like nano-graphite like structure. Figure 24 D and 24 E shows the graphene sheets scanned under 50% water + 50% ethanol mixture and methanol respectively.

Both shows the stacks of graphene sheets covering each other. Figure 24 F, 24 G, 24 H and 24 I are the HRTEM images of methanol, water, ethanol and IPA respectively. Except for the water condition, all shows the crystalline nature.

5.2 UV-Vis analysis

The UV-Vis spectra of few layers graphene UV laser scanned graphite are shown in figure 25. The 220 and 230 peaks shown in the figure belongs to π-π* transition of C-C bonds. While the

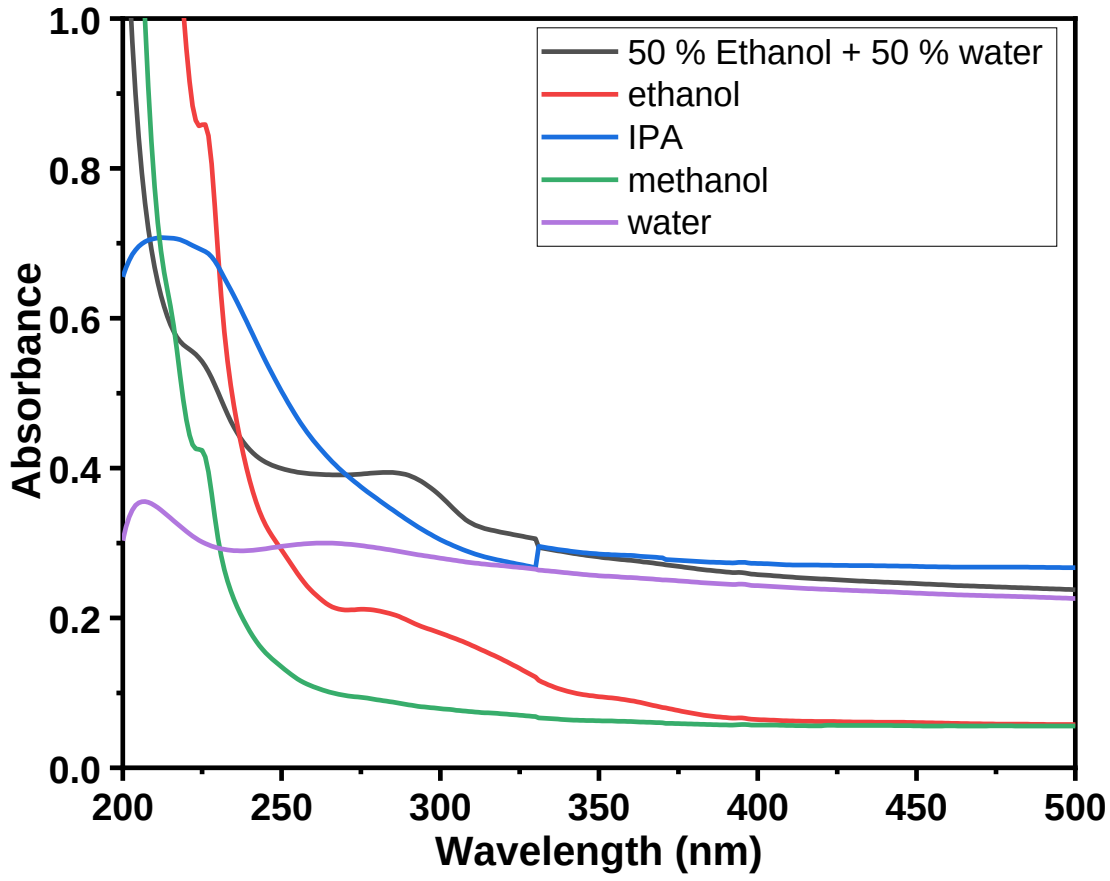

Figure 25: UV-Vis spectra of Water, IPA, Ethanol, 50% Water and 50% Ethanol, Methanol

absorption peaks at 270 nm and 280 nm confirm that the electronic conjugation within the graphene sheets.

5.3 Micro Raman analysis

For the confirmation of the presence of graphite, graphene oxide or graphene, Micro-Raman spectra has been taken. Figure 26 shows the Micro-Raman analysis spectra of laser scanned graphite in a different liquid environment. Graphene and its family can be easily recognized with

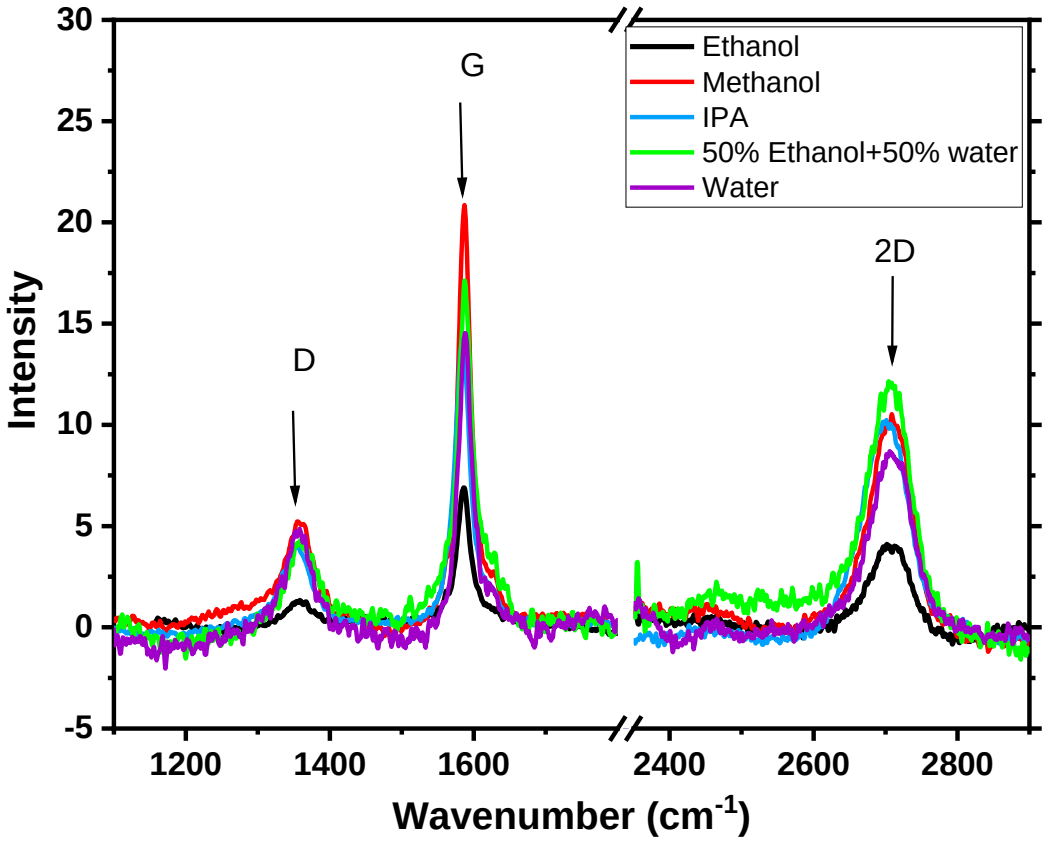

Figure 26: Micro-Raman spectra of Water, IPA, Ethanol, 50% Water and 50% Ethanol, Methanol

regards to orientation and the number of layers by inelastic light scattering. The Raman spectra of graphene shows the identity peaks in 1000-3000 cm^{-1} region. The three peaks of graphene lie at around ~1350, ~1560, ~2700 cm^{-1} named as D, G and 2D, respectively. The G peaks originate from the E2g phonon mode at the center of Brillouin zone and D peaks corresponds to Transverse optical mode (TO). The intensity of D peaks shows the amount of disorder in the graphene. 2D

peaks corresponds to the second order zone boundary phonons it shoes a strong appearance for the single layer structure[97-100]. The D, G and 2D bands in figure 26 show the presence of FLG in the liquid medium, which complements with TEM images. FLG produce in ethanol shows less defect than other liquid environments. Broad 2D peaks show the presence of 2 or more than 2 layers, as observed in TEM images.

5.4 Laser Microscope Analysis of laser ablated graphite plate

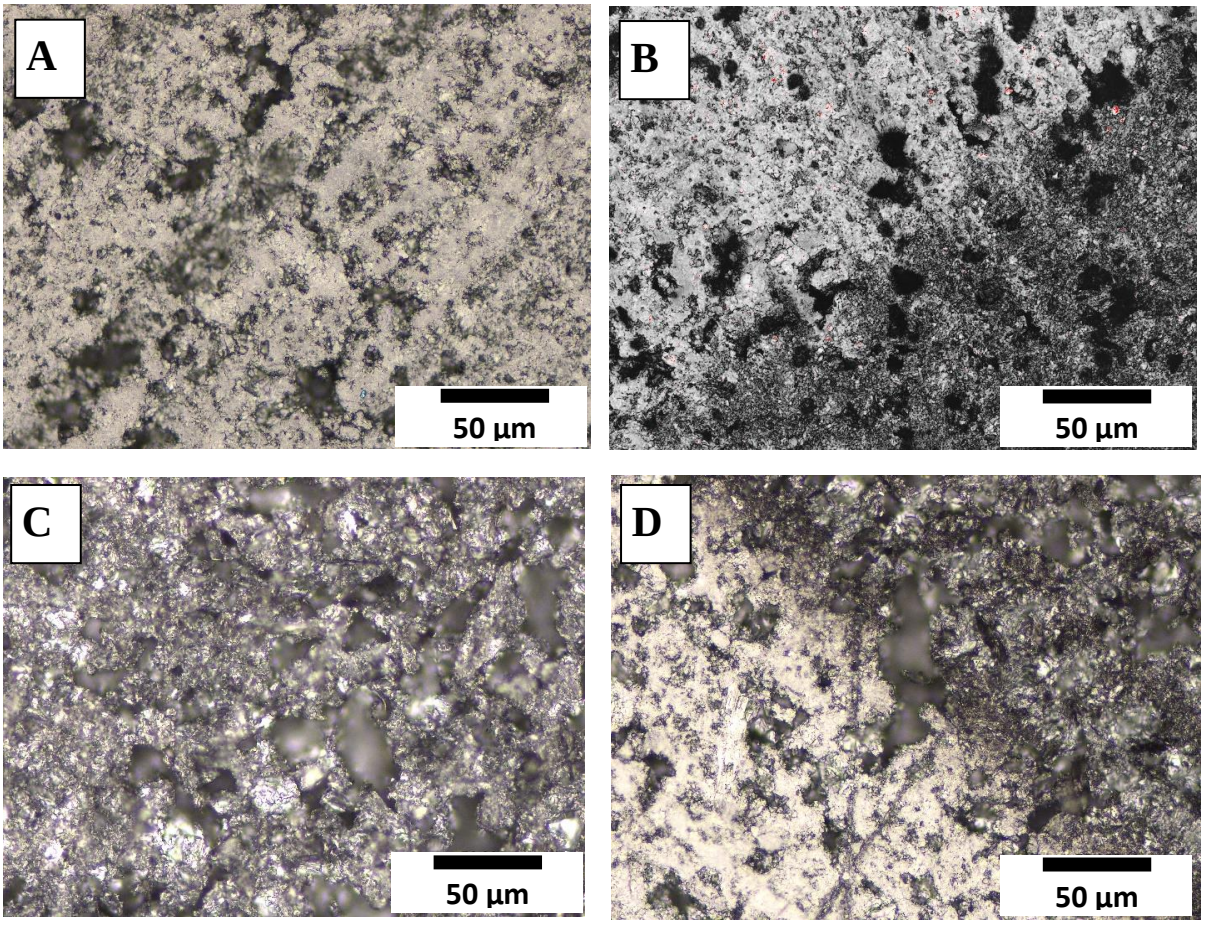

Figure 27: Optical laser microscopic image of graphite (A) before (B) in Water, (C) IPA, (D) Ethanol, 50% Water and 50% Ethanol, Methanol

Laser ablated graphite plate was observed using laser optical microscope to evaluate how much UV laser scanning was effective as well as laser effect on the surface. Figure 27 A shows the optical microscope image of graphite plate before laser scanning. The surface of graphite plate

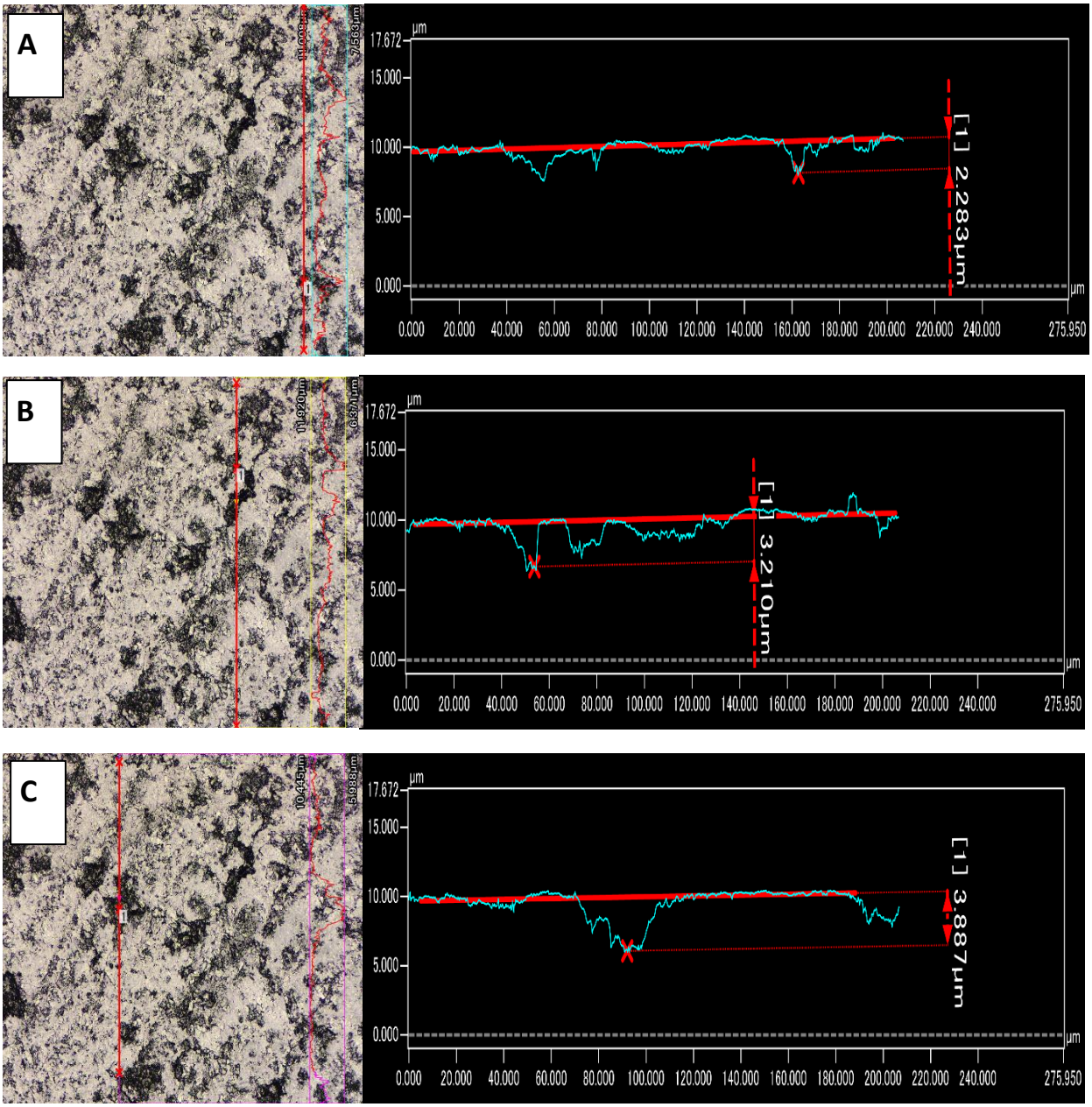

Figure 28: Surface analysis of Optical laser microscopic images of graphite before laser scanning

contains holes and hills, with irregular shapes and sizes. Figure 27 B, 27 C and 27 D shows the graphite plate after laser scanning under water IPA and Ethanol respectively. Each optical image taken after 3 hours of scanning. We also measure the depth of holes before and after laser scanning which shows in figure 28, figure 29, figure 31 and figure 32. Figure 28 shows the microscopic

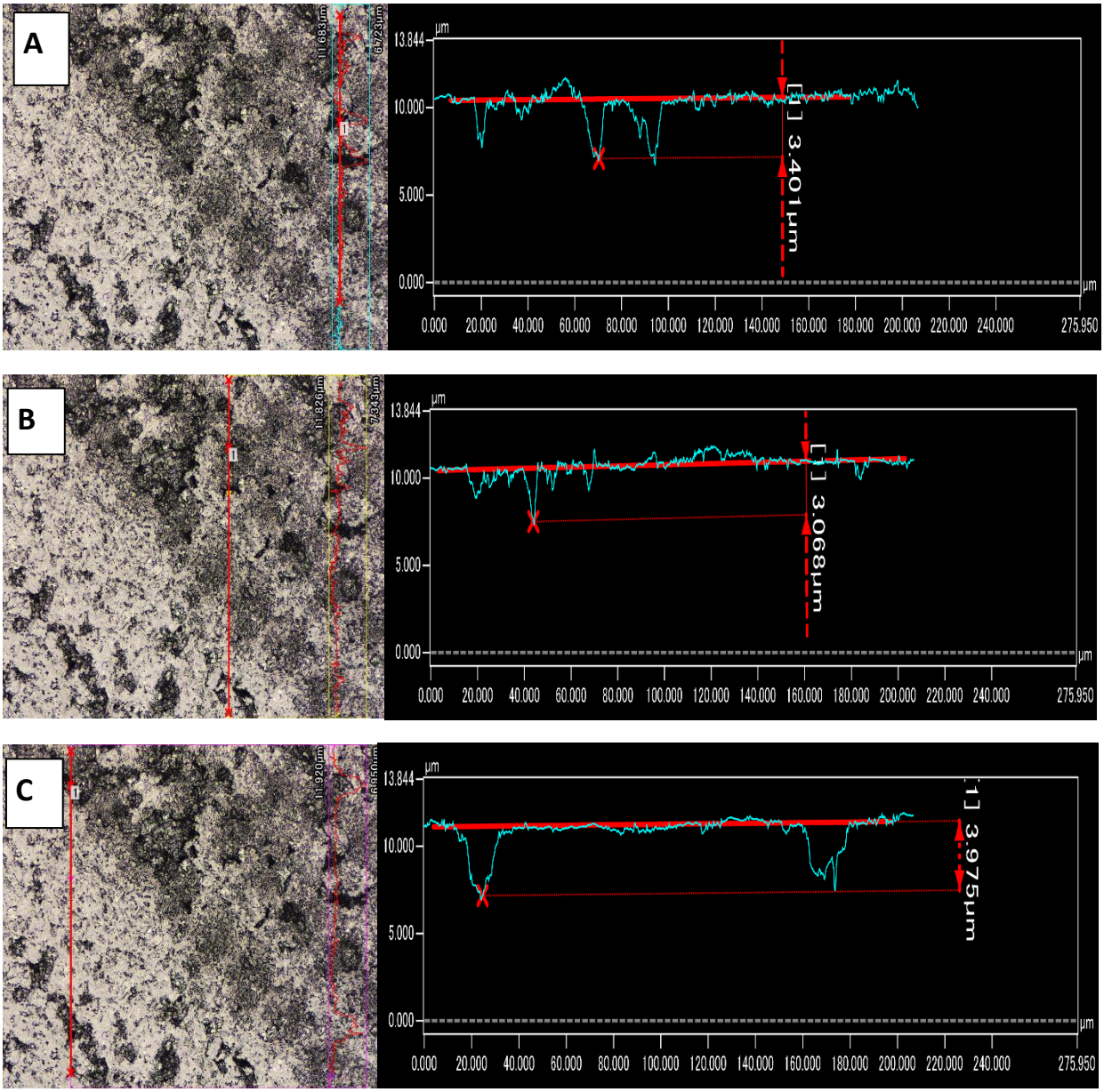

Figure 29: Optical laser microscopic image of graphite after laser scanning under ethanol

images of graphite before ablation and its surface analysis at different line. Figure 28 A, 28 B, 28 C shows uneven surface with holes and hills. The maximum observed depth is 3.88 µm and minimum depth is 2.2 µm as well as the average depth of holes in the graphite plate is 2.78 µm. By observing the spectra, the inside shape of holes is wide and irregular with many sub-holes. As observed in the figure 29, After getting laser ablation the surface become rougher and more hills

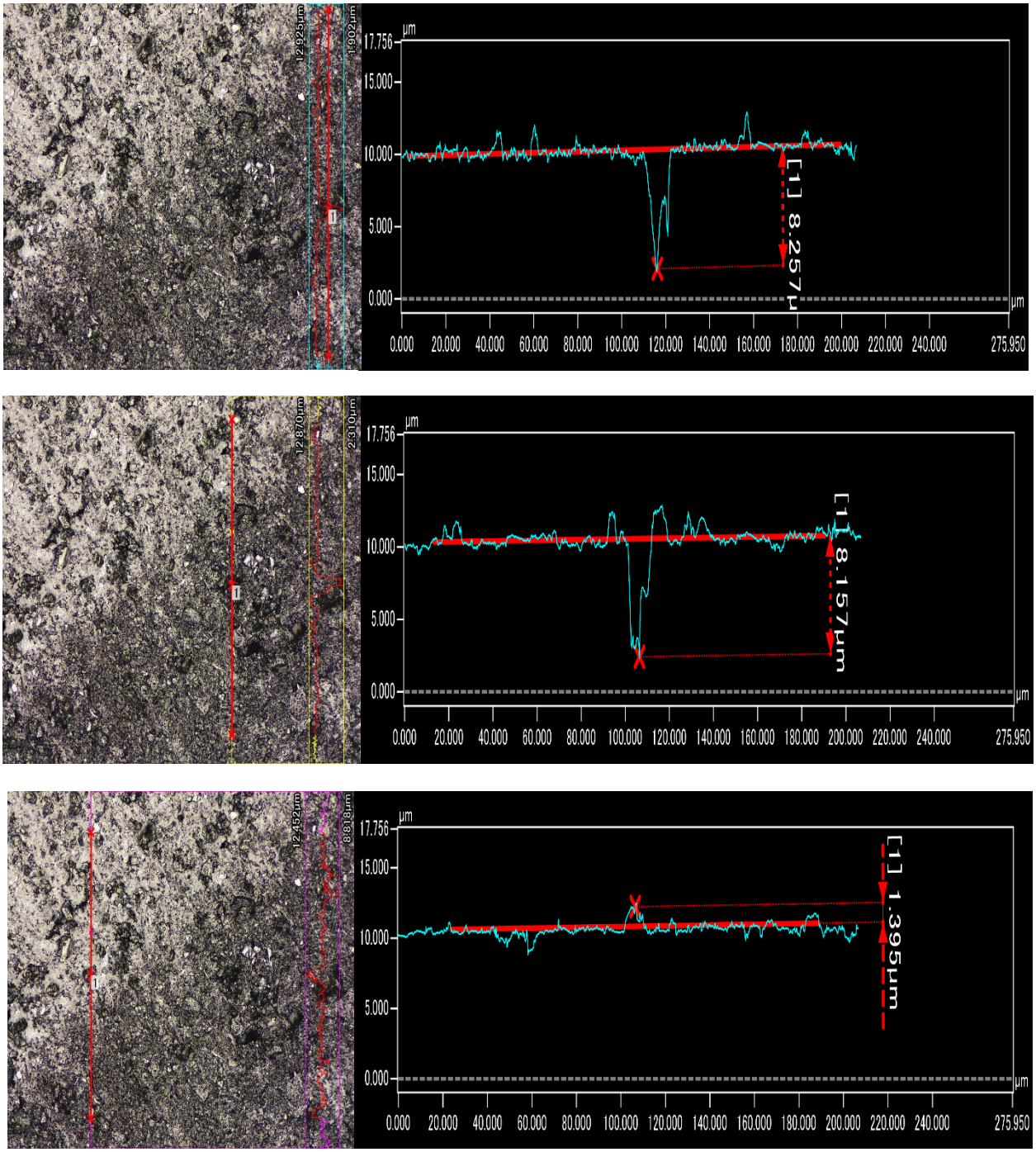

Figure 30: Optical laser microscopic images of graphite scanned under water

appear but the wideness of holes are getting closed due to removal of graphite upper surface. Figure 29 A mostly shows the ablated part of the graphene, in which depth measurement shows the sharp deeps and hills as well as the depths of holes are increased. Figure 29 B shows the line depth

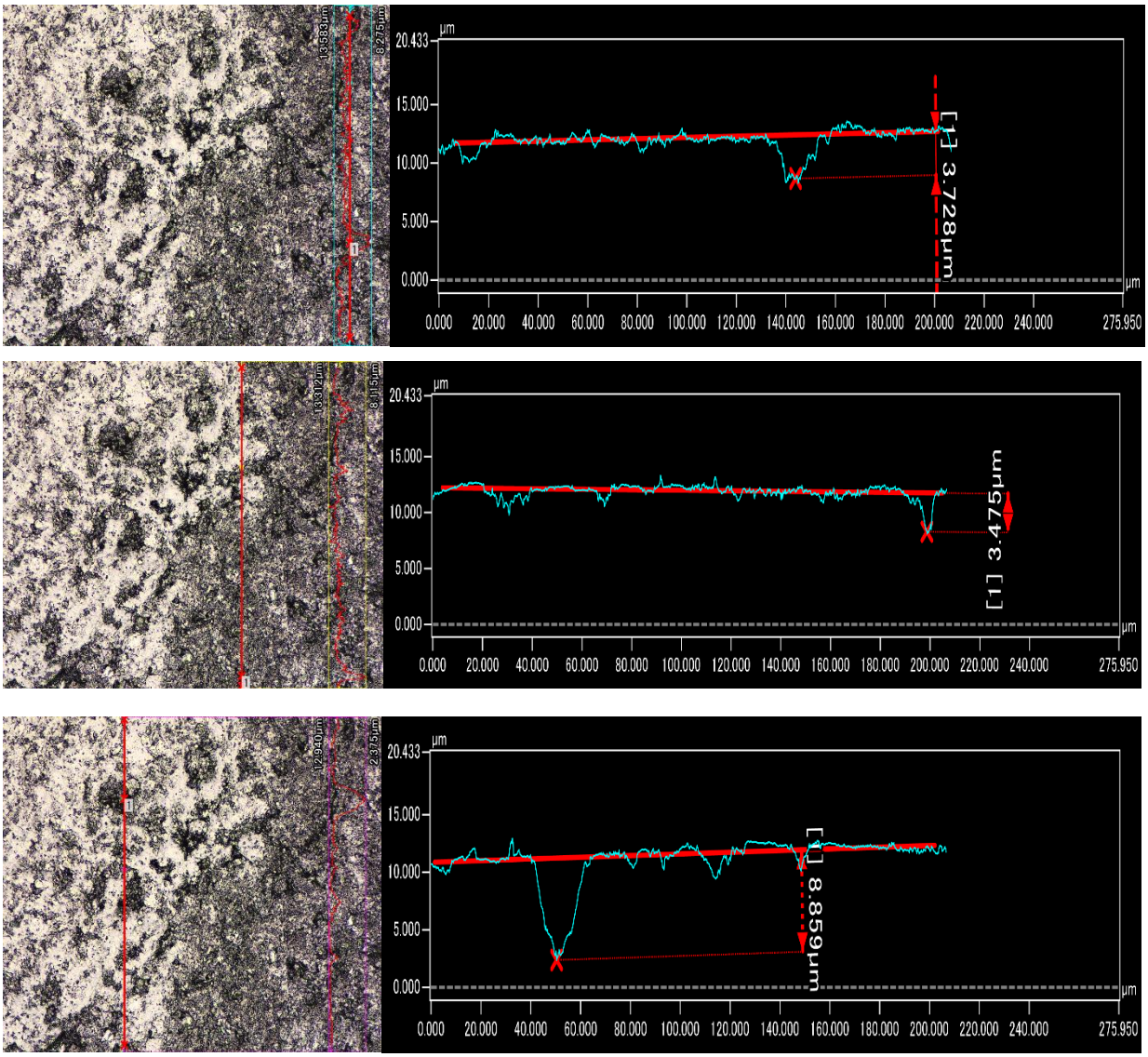

Figure 31: Optical laser microscopic image of graphite after laser scanning under isopropyl alcohol (IPA)

measurement along the interface of laser scanned part and non-scanned part. The average depth of holes is 2.4 µm. Figure 29 C shows the non-scanned part of the graphite plate which shows the uneven holes and rough surface. Figure 30 shows the laser optical microscopic images of graphite plate laser scanned under water. The laser scanning under water shows the deeper holes as compared to scanning under ethanol. The depths of holes are nearly doubling before laser scanning and laser scanning under ethanol. Whereas the figure 31 shows smoother surface compared to non-

scanned graphite plate and scanned graphite under water and ethanol. The number of hills and deeps are also decreased after laser scanning for 3 hours.

Chapter 6: Conclusion

A simple approach to prepare indium (III) selenide (In_2Se_3) nano-cubes using laser ablation in water. In addition, the detailed study on the field emission properties and charge carrier behavior of In_2Se_3 nano-cubes have been performed. We have used laser ablation in an aqueous medium to yield monodispersed nano-cubes structures of In_2Se_3. Although the synthesis was performed in an aqueous medium, the XRD, and micro-Raman analysis reveals that there is no phase change upon laser ablation. Furthermore, transient absorption spectroscopy shows the generation of intermediate trap states upon laser ablation, in which carriers have long lifetime near the conduction band. The In_2Se_3 nano-cubes planar emitter exhibits superior field emission properties, in particular, delivery of very high emission current density of ~2655 μA/cm² at a relatively moderate applied field of ~9.7 V/μm. Conclusively, the present method of laser ablation in aqueous medium, to synthesize monodispersed nanostructures possessing unique morphology, can be extended for other 2D materials. The prepared nano-cubes have enough prospective as nano-cubes emitter for practical applications in vacuum nano-microelectronic devices.

Novel In_2Se_3 nanocubes, In_2Se_3/Au, In_2Se_3/ZnO, and In_2Se_3/ZnO/Au catalytic systems were successfully synthesized using hydrothermal process and laser ablation in the liquid method. The optical, elemental, and photochemical properties were characterized, displaying the ternary composites potential implementation as a photocatalyst using ultrafast transient absorption method and photocatalytic reduction technique. The ternary composite (In_2Se_3/ZnO/Au) exhibited better performance than those of In_2Se_3 nanocubes, In_2Se_3/ZnO, and In_2Se_3 nanocubes decorated with AuNP. The improvement is due to (i) involvement of conduction band of ZnO in the ternary composite photocatalytic system, (ii) large surface area provided for the adsorption and

photocatalytic reaction, (iii) simultaneous excitation of both In_2Se_3 and AuNP and (iv) enhanced electron population in In_2Se_3 for faster electron transfer to MB.

The few layers graphene (FLG) successfully synthesized using ultraviolet laser scanning of graphite having wavelength 266 nm under various liquid environment. Water, ethanol, methanol and 50% ethanol + 50% water are the liquid medium were used to synthsised of FLG. Formation of FLG were successfully seen in TEM and crystallinity by HRTEM, the UV-Vis spectra show peaks belong to π-π^* transition peak of FLG as well as electronic conjugation within graphene sheet. Raman spectra reveal the disorder, orientation and number of layers by D, G, and 2D bands due to the inelastic light scattering. Optical laser microscopic images of graphite scanned under different liquid environment shows modifications on surface. Holes on the surface got dipper and sharp hills are produces due to laser scanning. Graphite scanned under IPA shows smoother surface than other graphite scanned under different liquid system.

Reference

1. Baldycheva, A., 2D material liquid crystals for optoelectronics and photonics. *Proceedings - International Conference Laser Optics 2018, ICLO 2018* **2018**, 194-194.
2. Cheng, L.; Wang, X.; Gong, F.; Liu, T.; Liu, Z., 2D Nanomaterials for Cancer Theranostic Applications. *Adv Mater* **2020,** *32* (13), e1902333.
3. Gao, G.; O'Mullane, A. P.; Du, A., 2D MXenes: A New Family of Promising Catalysts for the Hydrogen Evolution Reaction. *ACS Catalysis* **2016,** *7* (1), 494-500.
4. Hu, W.; Yang, J., Two-dimensional van der Waals heterojunctions for functional materials and devices. *Journal of Materials Chemistry C* **2017,** *5* (47), 12289-12297.
5. Majumdar, A.; Dodson, C. M.; Fryett, T. K.; Zhan, A.; Buckley, S.; Gerace, D., Hybrid 2D Material Nanophotonics: A Scalable Platform for Low-Power Nonlinear and Quantum Optics. *ACS Photonics* **2015,** *2* (8), 1160-1166.
6. Xiao, H.; Liu, S., 2D nanomaterials as lubricant additive: A review. *Materials & Design* **2017,** *135*, 319-332.
7. Zhang, H., Ultrathin Two-Dimensional Nanomaterials. *ACS Nano* **2015,** *9* (10), 9451-69.
8. Spear, J. C.; Ewers, B. W.; Batteas, J. D., 2D-nanomaterials for controlling friction and wear at interfaces. *Nano Today* **2015,** *10* (3), 301-314.
9. Druffel, D. L.; Woomer, A. H.; Kuntz, K. L.; Pawlik, J. T.; Warren, S. C., Electrons on the surface of 2D materials: from layered electrides to 2D electrenes. *Journal of Materials Chemistry C* **2017,** *5* (43), 11196-11213.
10. Xie, X.; Sarkar, D.; Liu, W.; Kang, J.; Marinov, O.; Deen, M. J.; Banerjee, K., Low-frequency noise in bilayer MoS(2) transistor. *ACS Nano* **2014,** *8* (6), 5633-40.
11. Mak, K. F.; Lee, C.; Hone, J.; Shan, J.; Heinz, T. F., Atomically thin MoS(2): a new direct-gap semiconductor. *Phys Rev Lett* **2010,** *105* (13), 136805.
12. Mueller, T.; Malic, E., Exciton physics and device application of two-dimensional transition metal dichalcogenide semiconductors. *npj 2D Materials and Applications* **2018,** *2* (1), 1-12.
13. Chen, X.; Qiu, Y.; Yang, H.; Liu, G.; Zheng, W.; Feng, W.; Cao, W.; Hu, W.; Hu, P., In-Plane Mosaic Potential Growth of Large-Area 2D Layered Semiconductors MoS2-MoSe2 Lateral Heterostructures and Photodetector Application. *ACS Appl Mater Interfaces* **2017,** *9* (2), 1684-1691.
14. Khan, M. A.; Rathi, S.; Park, J.; Lim, D.; Lee, Y.; Yun, S. J.; Youn, D. H.; Kim, G. H., Junctionless Diode Enabled by Self-Bias Effect of Ion Gel in Single-Layer MoS2 Device. *ACS Appl Mater Interfaces* **2017,** *9* (32), 26983-26989.
15. Mak, K. F.; Shan, J., Photonics and optoelectronics of 2D semiconductor transition metal dichalcogenides. *Nature Photonics* **2016,** *10* (4), 216-226.
16. Küpers, M.; Konze, P. M.; Meledin, A.; Mayer, J.; Englert, U.; Wuttig, M.; Dronskowski, R., Controlled Crystal Growth of Indium Selenide, In2Se3, and the Crystal Structures of α-In2Se3. *Inorganic Chemistry* **2018,** *57* (18), 11775-11781.
17. Rasmussen, A. M.; Teklemichael, S. T.; Mafi, E.; Gu, Y.; McCluskey, M. D., Pressure-induced phase transformation of In2Se3. *Applied Physics Letters* **2013,** *102* (6).
18. Li, S.; Yan, Y.; Zhang, Y.; Ou, Y.; Ji, Y.; Liu, L.; Yan, C.; Zhao, Y.; Yu, Z., Monophase γ-In2Se3 thin film deposited by magnetron radio-frequency sputtering. *Vacuum* **2014,** *99*, 228-232.
19. Li, T.; Wang, J.; Lai, J.; Zheng, X.; Liu, W.; Ji, J.; Liu, H.; Jin, Z., Multi-morphological growth of nano-structured In2Se3 by ambient pressure triethylene glycol based solution syntheses. *Journal of Alloys and Compounds* **2015,** *646*, 603-611.
20. Ider, M.; Pankajavalli, R.; Zhuang, W.; Shen, J. Y.; Anderson, T. J., Thermochemistry of the Cu2Se–In2Se3 system. *Journal of Alloys and Compounds* **2014,** *604*, 363-372.

21. Baek, C.-K.; Kang, D.; Kim, J.; Jin, B.; Rim, T.; Park, S.; Meyyappan, M.; Jeong, Y.-H.; Lee, J.-S., Improved performance of In2Se3 nanowire phase-change memory with SiO2 passivation. *Solid-State Electronics* **2013,** *80*, 10-13.
22. Wang, G.; Chen, G.; Li, W.; Zhang, W.; Zeng, C.; Zhao, W., Indium selenide as a saturable absorber for a laser. *Optical Materials Express* **2019,** *9* (2), 449-456.
23. Gao, W.; Liu, W.; Leng, Y.; Wang, X.; Wang, X.; Hu, B.; Yu, D.; Sang, Y.; Liu, H., In2S3 nanomaterial as a broadband spectrum photocatalyst to display significant activity. *Applied Catalysis B: Environmental* **2015,** *176-177*, 83-90.
24. Zhao, D.; Sheng, G.; Chen, C.; Wang, X., Enhanced photocatalytic degradation of methylene blue under visible irradiation on graphene@TiO2 dyade structure. *Applied Catalysis B: Environmental* **2012,** *111-112*, 303-308.
25. Ye, D.; Moussa, S.; Ferguson, J. D.; Baski, A. A.; El-Shall, M. S., Highly efficient electron field emission from graphene oxide sheets supported by nickel nanotip arrays. *Nano Lett* **2012,** *12* (3), 1265-8.
26. Shen, J.; Zhu, Y.; Yang, X.; Zong, J.; Zhang, J.; Li, C., One-pot hydrothermal synthesis of graphenequantum dots surface-passivated by polyethylene glycol and their photoelectric conversion under near-infrared light. *New J. Chem.* **2012,** *36* (1), 97-101.
27. Wang, L.; Wang, Y.; Xu, T.; Liao, H.; Yao, C.; Liu, Y.; Li, Z.; Chen, Z.; Pan, D.; Sun, L.; Wu, M., Gram-scale synthesis of single-crystalline graphene quantum dots with superior optical properties. *Nature Communications* **2014,** *5* (1), 5357.
28. Randviir, E. P.; Brownson, D. A. C.; Banks, C. E., A decade of graphene research: production, applications and outlook. *Materials Today* **2014,** *17* (9), 426-432.
29. Yu, H.; Zhang, B.; Bulin, C.; Li, R.; Xing, R., High-efficient Synthesis of Graphene Oxide Based on Improved Hummers Method. *Scientific Reports* **2016,** *6* (1), 36143.
30. Li, M.; Liu, D.; Wei, D.; Song, X.; Wei, D.; Wee, A. T. S., Controllable Synthesis of Graphene by Plasma-Enhanced Chemical Vapor Deposition and Its Related Applications. *Advanced Science* **2016,** *3* (11), 1600003.
31. Zaaba, N. I.; Foo, K. L.; Hashim, U.; Tan, S. J.; Liu, W.-W.; Voon, C. H., Synthesis of Graphene Oxide using Modified Hummers Method: Solvent Influence. *Procedia Engineering* **2017,** *184*, 469-477.
32. Wang, H.; Robinson, J. T.; Diankov, G.; Dai, H., Nanocrystal Growth on Graphene with Various Degrees of Oxidation. *J. Am. Chem. Soc.* **2010,** *132*, 3270.
33. Pramanik, A.; Karmakar, S.; Kumbhakar, P.; Biswas, S.; Sarkar, R.; Kumbhakar, P., Synthesis of bilayer graphene nanosheets by pulsed laser ablation in liquid and observation of its tunable nonlinearity. *Applied Surface Science* **2020,** *499*, 143902-143902.
34. Li, X.; Wang, Q.; Zhao, Y.; Wu, W.; Chen, J.; Meng, H., Green synthesis and photo-catalytic performances for ZnO-reduced graphene oxide nanocomposites. *J Colloid Interface Sci* **2013,** *411*, 69-75.
35. Furube, A.; Du, L.; Hara, K.; Katoh, R.; Tachiya, M., Ultrafast plasmon-induced electron transfer from gold nanodots into TiO2 nanoparticles. *J Am Chem Soc* **2007,** *129* (48), 14852-3.
36. Du, L.; Furube, A.; Hara, K.; Katoh, R.; Tachiya, M., Ultrafast plasmon induced electron injection mechanism in gold–TiO2 nanoparticle system. *Journal of Photochemistry and Photobiology C: Photochemistry Reviews* **2013,** *15*, 21-30.
37. Sylvestre, J.-P.; Poulin, S.; Kabashin, A. V.; Sacher, E.; Meunier, M.; Luong, J. H. T., Surface Chemistry of Gold Nanoparticles Produced by Laser Ablation in Aqueous Media. *The Journal of Physical Chemistry B* **2004,** *108* (43), 16864-16869.
38. M., C. Y.; L., L. M.; Y., L. T.; Y., L. H.; M., L. C.; C., W. Y.; Y., J. J., Field emission properties of gold nanoparticle-decorated ZnO nanopillars. *ACS Appl Mater Interfaces* **2012,** *4* (12), 6676-82.

39. Hu, J.; Karam, T. E.; Blake, G. A.; Zewail, A. H., Ultrafast lattice dynamics of single crystal and polycrystalline gold nanofilms☆. *Chemical Physics Letters* **2017,** *683*, 258-261.
40. Larm, N. E.; Essner, J. B.; Pokpas, K.; Canon, J. A.; Jahed, N.; Iwuoha, E. I.; Baker, G. A., Room-Temperature Turkevich Method: Formation of Gold Nanoparticles at the Speed of Mixing Using Cyclic Oxocarbon Reducing Agents. *The Journal of Physical Chemistry C* **2018,** *122* (9), 5105-5118.
41. Nasiri, P.; Doranian, D.; Sari, A. H., Synthesis of Au/Si nanocomposite using laser ablation method. *Optics & Laser Technology* **2019,** *113* (November 2018), 217-224.
42. Turkevich, J.; Stevenson, P. C.; Hillier, J., A study of the nucleation and growth processes in the synthesis of colloidal gold. *Discussions of the Faraday Society* **1951,** *11* (0), 55-75.
43. Baigent, C. L.; Müller, G., A colloidal gold prepared with ultrasonics. *Experientia* **1980,** *36* (4), 472-473.
44. Brust, M.; Walker, M.; Bethell, D.; Schiffrin, D. J.; Whyman, R., Synthesis of thiol-derivatised gold nanoparticles in a two-phase Liquid–Liquid system. *Journal of the Chemical Society, Chemical Communications* **1994,** (7), 801-802.
45. Martin, M. N.; Basham, J. I.; Chando, P.; Eah, S.-K., Charged Gold Nanoparticles in Non-Polar Solvents: 10-min Synthesis and 2D Self-Assembly. *Langmuir* **2010,** *26* (10), 7410-7417.
46. Niu, Z.; Li, Y., Removal and Utilization of Capping Agents in Nanocatalysis. *Chemistry of Materials* **2014,** *26* (1), 72-83.
47. Suntako, R., Effect of zinc oxide nanoparticles synthesized by a precipitation method on mechanical and morphological properties of the CR foam. *Bulletin of Materials Science* **2015,** *38* (4), 1033-1038.
48. Hezma, A. M.; Rajeh, A.; Mannaa, M. A., An insight into the effect of zinc oxide nanoparticles on the structural, thermal, mechanical properties and antimicrobial activity of Cs/PVA composite. *Colloids and Surfaces A: Physicochemical and Engineering Aspects* **2019,** *581*, 123821.
49. Xu, Z.; Zheng, L.; Wen, S.; Liu, L., Graphene oxide-supported zinc oxide nanoparticles for chloroprene rubber with improved crosslinking network and mechanical properties. *Composites Part A: Applied Science and Manufacturing* **2019,** *124*, 105492.
50. Lamas, D. G.; Lascalea, G. E.; de Reca, N. E. W., Synthesis and characterization of nanocrystalline powders for partially stabilized zirconia ceramics. *Journal of the European Ceramic Society* **1998,** *18* (9), 1217-1221.
51. Chang, S.-S.; Yoon, S. O.; Park, H. J.; Sakai, A., Luminescence properties of Zn nanowires prepared by electrochemical etching. *Materials Letters* **2002,** *53* (6), 432-436.
52. Wu, J. J.; Liu, S. C., Low-Temperature Growth of Well-Aligned ZnO Nanorods by Chemical Vapor Deposition. *Advanced Materials* **2002,** *14* (3), 215-218.
53. Usui, H.; Shimizu, Y.; Sasaki, T.; Koshizaki, N., Photoluminescence of ZnO Nanoparticles Prepared by Laser Ablation in Different Surfactant Solutions. *The Journal of Physical Chemistry B* **2005,** *109* (1), 120-124.
54. Scarisoreanu, N.; Matei, D. G.; Dinescu, G.; Epurescu, G.; Ghica, C.; Nistor, L. C.; Dinescu, M., Properties of ZnO thin films prepared by radio-frequency plasma beam assisted laser ablation. *Applied Surface Science* **2005,** *247* (1), 518-525.
55. Ni, Y.-h.; Wei, X.-w.; Hong, J.-m.; Ye, Y., Hydrothermal preparation and optical properties of ZnO nanorods. *Materials Science and Engineering: B* **2005,** *121* (1), 42-47.
56. Ristić, M.; Musić, S.; Ivanda, M.; Popović, S., Sol–gel synthesis and characterization of nanocrystalline ZnO powders. *Journal of Alloys and Compounds* **2005,** *397* (1), L1-L4.
57. Fang, X.; Li, J.; Zhao, D.; Shen, D.; Li, B.; Wang, X., Phosphorus-Doped p-Type ZnO Nanorods and ZnO Nanorod p−n Homojunction LED Fabricated by Hydrothermal Method. *The Journal of Physical Chemistry C* **2009,** *113* (50), 21208-21212.

58. Dell'Aglio, M.; Gaudiuso, R.; De Pascale, O.; De Giacomo, A., Mechanisms and processes of pulsed laser ablation in liquids during nanoparticle production. *Applied Surface Science* **2015,** *348*, 4-9.
59. Venkata Subbaiah, Y. P.; Saji, K. J.; Tiwari, A., Atomically Thin MoS2: A Versatile Nongraphene 2D Material. *Advanced Functional Materials* **2016,** *26* (13), 2046-2069.
60. Tsuji, T.; Iryo, K.; Nishimura, Y.; Tsuji, M., Preparation of metal colloids by a laser ablation technique in solution: influence of laser wavelength on the ablation efficiency (II). *Journal of Photochemistry and Photobiology A: Chemistry* **2001,** *145* (3), 201-207.
61. Guillong, M.; Horn, I.; Günther, D., A comparison of 266 nm, 213 nm and 193 nm produced from a single solid state Nd:YAG laser for laser ablation ICP-MS. *J. Anal. At. Spectrom.* **2003,** *18* (10), 1224-1230.
62. Huang, K. C.; McCall, J.; Wang, P.; Liao, C. S.; Eakins, G.; Cheng, J. X.; Yang, C., High-Speed Spectroscopic Transient Absorption Imaging of Defects in Graphene. *Nano Lett* **2018,** *18* (2), 1489-1497.
63. Tao, X.; Mafi, E.; Gu, Y., Ultrafast carrier dynamics in single-crystal In2Se3 thin layers. *Applied Physics Letters* **2013,** *103* (19), 3-7.
64. Asahi, T.; Furube, A.; Fukumura, H.; Ichikawa, M.; Masuhara, H., Development of a femtosecond diffuse reflectance spectroscopic system, evaluation of its temporal resolution, and applications to organic powder systems. *Review of Scientific Instruments* **1998,** *69* (2), 361-371.
65. Katayama, T.; Suenaga, H.; Okuhata, T.; Masuo, S.; Tamai, N., Unraveling the Ultrafast Exciton Relaxation and Hidden Energy State in CH3NH3PbBr3 Nanoparticles. *The Journal of Physical Chemistry C* **2018,** *122* (9), 5209-5214.
66. Ahmad, M.; Sun, H.; Zhu, J., Enhanced Photoluminescence and Field-Emission Behavior of Vertically Well Aligned Arrays of In-Doped ZnO Nanowires. *ACS Applied Materials & Interfaces* **2011,** *3* (4), 1299-1305.
67. Charlier, J. C.; Terrones, M.; Baxendale, M.; Meunier, V.; Zacharia, T.; Rupesinghe, N. L.; Hsu, W. K.; Grobert, N.; Terrones, H.; Amaratunga, G. A. J., Enhanced Electron Field Emission in B-doped Carbon Nanotubes. *Nano Letters* **2002,** *2* (11), 1191-1195.
68. Chubenko, O.; Baturin, S. S.; Kovi, K. K.; Sumant, A. V.; Baryshev, S. V., Locally Resolved Electron Emission Area and Unified View of Field Emission from Ultrananocrystalline Diamond Films. *ACS Appl Mater Interfaces* **2017,** *9* (38), 33229-33237.
69. Suryawanshi, S. R.; Bankar, P. K.; More, M. A.; Late, D. J., Vapour–liquid–solid growth of one-dimensional In2Se3 nanostructures and their promising field emission behaviour. *RSC Advances* **2015,** *5* (80), 65274-65282.
70. Wang, Q.; Yu, K.; Xu, F.; Wu, J.; Xu, Y. e.; Zhu, Z., Synthesis and field-emission properties of In2O3 nanostructures. *Materials Letters* **2008,** *62* (17-18), 2710-2713.
71. Fowler, R. H.; Nordheim, L., Electron emission in intense electric fields. *Proceedings of the Royal Society of London. Series A, Containing Papers of a Mathematical and Physical Character* **1928,** *119* (781), 173-181.
72. koinkar, P. Field emission studies of CVD diamond thin films. K.B.C. North Maharashtra University, India, 2005.
73. Dusane, P. R.; Thombare, B. R.; Bankar, P. K.; Lole, G.; Gavhane, D.; Khedkar, C. V.; Nagrare, B.; Salunkhe, A.; Kolhe, P.; Choudhary, R. J.; Phase, D. M.; More, M. A.; Patil, S. I., Vertically aligned ultrathin MoSe2 nanoflakes grown on carbon cloth and its field emission behaviour. *Materials Research Bulletin* **2019,** *116*, 67-71.
74. Iemmo, L.; Di Bartolomeo, A.; Giubileo, F.; Luongo, G.; Passacantando, M.; Niu, G.; Hatami, F.; Skibitzki, O.; Schroeder, T., Graphene enhanced field emission from InP nanocrystals. *Nanotechnology* **2017,** *28* (49), 495705.

75. Shinde, D. R.; Chavan, P. G.; Sen, S.; Joag, D. S.; More, M. A.; Gadkari, S. C.; Gupta, S. K., Enhanced field-emission from SnO2:WO(2.72) nanowire heterostructures. *ACS Appl Mater Interfaces* **2011,** *3* (12), 4730-5.
76. Pak, C.; Woo, J. Y.; Lee, K.; Kim, W. D.; Yoo, Y.; Lee, D. C., Extending the Limit of Low-Energy Photocatalysis: Dye Reduction with PbSe/CdSe/CdS Core/Shell/Shell Nanocrystals of Varying Morphologies under Infrared Irradiation. *The Journal of Physical Chemistry C* **2012,** *116* (48), 25407-25414.
77. Singh, A. K.; Mathew, K.; Zhuang, H. L.; Hennig, R. G., Computational Screening of 2D Materials for Photocatalysis. *J Phys Chem Lett* **2015,** *6* (6), 1087-98.
78. Xiong, J.; Di, J.; Xia, J.; Zhu, W.; Li, H., Surface Defect Engineering in 2D Nanomaterials for Photocatalysis. *Advanced Functional Materials* **2018,** *28* (39), 1801983.
79. Pérez-Larios, A.; Lopez, R.; Hernández-Gordillo, A.; Tzompantzi, F.; Gómez, R.; Torres-Guerra, L. M., Improved hydrogen production from water splitting using TiO2–ZnO mixed oxides photocatalysts. *Fuel* **2012,** *100*, 139-143.
80. Ida, S.; Ishihara, T., Recent Progress in Two-Dimensional Oxide Photocatalysts for Water Splitting. *The Journal of Physical Chemistry Letters* **2014,** *5* (15), 2533-2542.
81. Moniz, S. J. A.; Shevlin, S. A.; Martin, D. J.; Guo, Z.-X.; Tang, J., Visible-light driven heterojunction photocatalysts for water splitting – a critical review. *Energy & Environmental Science* **2015,** *8* (3), 731-759.
82. Zhou, X.; Dong, H., A Theoretical Perspective on Charge Separation and Transfer in Metal Oxide Photocatalysts for Water Splitting. *ChemCatChem* **2019,** *11* (16), 3688-3715.
83. Dhongade, S.; Mutadak, P. R.; Deore, A. B.; More, M. A.; Furube, A.; Koinkar, P., In2Se3 Nanocubes as High Current Density Cold Cathode Materials. *ACS Applied Nano Materials* **2020,** *3* (10), 9749-9758.
84. Uchida, K.; Kubo, T.; Yamanaka, D.; Furube, A.; Matsuzaki, H.; Nishii, R.; Sakagami, Y.; Abulikemu, A.; Kamada, K., Synthesis, crystal structure, and photophysical properties of 2,9-disubstituted peropyrene derivatives. *Canadian Journal of Chemistry* **2017,** *95* (4), 432-444.
85. Vilaplana, R.; Parra, S. G.; Jorge-Montero, A.; Rodriguez-Hernandez, P.; Munoz, A.; Errandonea, D.; Segura, A.; Manjon, F. J., Experimental and Theoretical Studies on alpha-In2Se3 at High Pressure. *Inorg Chem* **2018,** *57* (14), 8241-8252.
86. Wiley, B.; Sun, Y.; Mayers, B.; Xia, Y., Shape-Controlled Synthesis of Metal Nanostructures: The Case of Silver. *Chemistry – A European Journal* **2005,** *11* (2), 454-463.
87. Xia, Y.; Xia, X.; Peng, H.-C., Shape-Controlled Synthesis of Colloidal Metal Nanocrystals: Thermodynamic versus Kinetic Products. *Journal of the American Chemical Society* **2015,** *137* (25), 7947-7966.
88. Botcha, V. D.; Hong, Y.; Huang, Z.; Li, Z.; Liu, Q.; Wu, J.; Lu, Y.; Liu, X., Growth and thermal properties of various In2Se3 nanostructures prepared by single step PVD technique. *Journal of Alloys and Compounds* **2019,** *773*, 698-705.
89. Liu, P.; Yu, S.; Fan, W.; Shi, W., A new inorganic-organic hybrid In2Se3(en) as hollow nanospheres: hydrothermal synthesis and near-infrared photoluminescence properties. *Dalton Trans* **2013,** *42* (8), 2887-93.
90. Ho, C.-H.; Lin, C.-H.; Wang, Y.-P.; Chen, Y.-C.; Chen, S.-H.; Huang, Y.-S., Surface Oxide Effect on Optical Sensing and Photoelectric Conversion of α-In2Se3 Hexagonal Microplates. *ACS Applied Materials & Interfaces* **2013,** *5* (6), 2269-2277.
91. Zhang, L.; Xing, J.; Wen, X.; Chai, J.; Wang, S.; Xiong, Q., Plasmonic heating from indium nanoparticles on a floating microporous membrane for enhanced solar seawater desalination. *Nanoscale* **2017,** *9* (35), 12843-12849.

92. Al-Tabbakh, A. A., The behavior of the Fowler–Nordheim plot for ZnO–Cu virtual emitter arrays. *Indian Journal of Physics* **2019,** *93* (1), 41-46.
93. Diallo, A.; Ngom, B. D.; Park, E.; Maaza, M., Green synthesis of ZnO nanoparticles by Aspalathus linearis: Structural & optical properties. *Journal of Alloys and Compounds* **2015,** *646*, 425-430.
94. Taguchi, A.; Yu, J.; Saitoh, K., 4.02 - Tip Enhanced Raman Microscopy. In *Comprehensive Nanoscience and Nanotechnology (Second Edition)*, Andrews, D. L.; Lipson, R. H.; Nann, T., Eds. Academic Press: Oxford, 2019; pp 13-32.
95. Aljawfi, R. N.; Alam, M. J.; Rahman, F.; Ahmad, S.; Shahee, A.; Kumar, S., Impact of annealing on the structural and optical properties of ZnO nanoparticles and tracing the formation of clusters via DFT calculation. *Arabian Journal of Chemistry* **2020,** *13* (1), 2207-2218.
96. Du, L. C.; Xi, W. D.; Zhang, J. B.; Matsuzaki, H.; Furube, A., Electron transfer dynamics and yield from gold nanoparticle to different semiconductors induced by plasmon band excitation. *Chemical Physics Letters* **2018,** *701*, 126-130.
97. Ferrari, A. C.; Meyer, J. C.; Scardaci, V.; Casiraghi, C.; Lazzeri, M.; Mauri, F.; Piscanec, S.; Jiang, D.; Novoselov, K. S.; Roth, S.; Geim, A. K., Raman Spectrum of Graphene and Graphene Layers. *Physical Review Letters* **2006,** *97* (18), 187401.
98. Schedin, F.; Lidorikis, E.; Lombardo, A.; Kravets, V. G.; Geim, A. K.; Grigorenko, A. N.; Novoselov, K. S.; Ferrari, A. C., Surface-Enhanced Raman Spectroscopy of Graphene. *ACS Nano* **2010,** *4* (10), 5617-5626.
99. Ferrari, A. C.; Basko, D. M., Raman spectroscopy as a versatile tool for studying the properties of graphene. *Nature Nanotechnology* **2013,** *8* (4), 235-246.
100. Malard, L. M.; Pimenta, M. A.; Dresselhaus, G.; Dresselhaus, M. S., Raman spectroscopy in graphene. *Physics Reports* **2009,** *473* (5), 51-87.

Research activity

Academic Research paper:

1. Siddhant Dhongade, Pallavi R. Mutadak, Amol B. Deore, Mahendra A. More, Akihiro Furube and Pankaj Koinkar: **"In_2Se_3 Nanocubes as High Current Density Cold Cathode Materials"** *ACS Applied Nano Materials 2020, 3, 9749-9758.*

2. Siddhant Dhongade, Yutaro Maki, Tetsuro Katayama, Pankaj Koinkar, and Akihiro Furube: "**Charge Separation Dynamics in In_2Se_3/ZnO/Au Ternary System for Enhanced Photocatalytic Degradation of Methylene Blue under Visible Light"** *Journal of Photochemistry & Photobiology, A: Chemistry* **(under review)**.

Proceedings of International Conference

1. Siddhant Dhongade, Akihiro Furube, Pankaj Koinkar: "**Fabrication of In_2Se_3 nanocubes via laser ablation in liquid**" *2nd International Conference on Nanomaterials & Advanced Composites (August 9-11 2019) D6 Inorganic Nanomaterials (I): Oral session.*
2. Siddhant Dhongade, Akihiro Furube, Pankaj Koinkar: **"Development of gold (Au) decorated In_2Se_3 nanocubes via laser ablation in liquid"** International Forum on Advanced Technologies (IFAT) March 2020, Tokushima University, Japan.

Proceedings of Domestic Conference

1. Siddhant Dhongade, Akihiro Furube, Pankaj Koinkar, Mahendra A. More, **"Enhanced field emission from indium (III) selenide nanocubes synthesized by laser ablation in liquid"** *The Japan Society of Applied Physics spring meeting 2020*, 4.3 Lasers and laser materials processing, online conference ID 11a-Z16-5.

Awards

1. '**National Overseas Scholarship**' Government of India, received from April 2018 to March 2021.
2. **Best paper presentation Award**; Siddhant Dhongade, Akihiro Furube, Pankaj Koinkar: "**Fabrication of In_2Se_3 nanocubes via laser ablation in liquid**" *2nd International Conference on Nanomaterials & Advanced Composites (August 9-11 2019).*

Research internship

1. **'Laser scan ablation of graphite plate'** National Institute of Advanced Industrial Science and Technology, Tsukuba, 20 August 2019 to 30 September 2019.
2. **'Preparation of graphene from graphite by UV Laser scanning'** National Institute of Advanced Industrial Science and Technology, Tsukuba, 7 December 2020 to 11 December 2020.